The Astrophysical Journal, 972:194 (27pp), 2024 September 10 https://doi.org/10.3847/1538-4357/ad5a7c

SN 2022oqm: A Bright and Multipeaked Calcium-rich Transient

S. Karthik Yadavalli[1], V. Ashley Villar[1], Luca Izzo[2], Yossef Zenati[3,29], Ryan J. Foley[4], J. Craig Wheeler[5], Charlotte R. Angus[2], Dominik Bánhidi[6], Katie Auchettl[4,7], Barna Imre Bíró[6,8], Attila Bódi[9,10,11], Zsófia Bodola[12], Thomas de Boer[13], Kenneth C. Chambers[13], Ryan Chornock[14], David A. Coulter[4], István Csányi[6], Borbála Cseh[9,10,15], Srujan Dandu[4], Kyle W. Davis[4], Connor Braden Dickinson[4], Diego Farias[2], Joseph Farah[16,17], Christa Gall[2], Hua Gao[13], D. Andrew Howell[16,17], Wynn V. Jacobson-Galan[14], Nandita Khetan[2,18], Charles D. Kilpatrick[19], Réka Könyves-Tóth[9,10,12,20], Levente Kriskovics[9,10], Natalie LeBaron[14], Kayla Loertscher[4], X. K. Le Saux[4], Raffaella Margutti[14,21], Eugene A. Magnier[13], Curtis McCully[16], Peter McGill[4], Hao-Yu Miao[22], Megan Newsome[16,17], Estefania Padilla Gonzalez[16,17], András Pál[9,10,23], Boróka H. Pál[12], Yen-Chen Pan[22], Collin A. Politsch[24], Conor L. Ransome[1], Enrico Ramirez-Ruiz[4], Armin Rest[3,25], Sofia Rest[3,25], Olivia Robinson[4], Huei Sears[19,26], Jackson Scheer[27], Ádám Sódor[9,10,11], Jonathan Swift[27], Péter Székely[8,12], Róbert Szakáts[9,10], Tamás Szalai[8,12,28], Kirsty Taggart[4], Giacomo Terreran[16,17], Padma Venkatraman[14], József Vinkó[5,9,10,12,23], Grace Yang[27], and Henry Zhou[27]

[1] Center for Astrophysics | Harvard & Smithsonian, 60 Garden Street, Cambridge, MA 02138-1516, USA
[2] DARK, Niels Bohr Institute, University of Copenhagen, Jagtvej 128, 2200 Copenhagen, Denmark
[3] Physics and Astronomy Department, Johns Hopkins University, Baltimore, MD 21218, USA
[4] Department of Astronomy and Astrophysics, University of California, Santa Cruz, CA 95064, USA
[5] Department of Astronomy, University of Texas at Austin, 2515 Speedway Stop C1400, Austin, TX 78712-1205, USA
[6] Baja Astronomical Observatory of University of Szeged, Szegedi út Kt. 766, Baja 6500, Hungary
[7] School of Physics, The University of Melbourne, VIC 3010, Australia
[8] HUN-REN–SZTE Stellar Astrophysics Research Group, Szegedi út Kt. 766, Baja 6500, Hungary
[9] Konkoly Observatory, Research Centre for Astronomy and Earth Sciences, Budapest, Konkoly Thege Miklós út 15-17, 1121, Hungary
[10] CSFK, MTA Centre of Excellence, Budapest, Konkoly Thege Miklós út 15-17, 1121, Hungary
[11] MTA CSFK Lendület Near-Field Cosmology Research Group, Konkoly Thege Miklós út 15-17, Budapest 1121, Hungary
[12] Department of Experimental Physics, Institute of Physics, University of Szeged, Dóm tér 9, Szeged 6720, Hungary
[13] Institute for Astronomy, University of Hawaii, 2680 Woodlawn Drive, Honolulu, HI 96822, USA
[14] Department of Astronomy, University of California, Berkeley, CA 94720-3411, USA
[15] MTA CSFK Lendület "Momentum" Milky Way Research Group, Hungary
[16] Las Cumbres Observatory Global Telescope Network, Goleta, CA 93117, USA
[17] Department of Physics, University of California, Santa Barbara, CA 93106, USA
[18] School of Mathematics and Physics, University of Queensland, 4101, Australia
[19] Center for Interdisciplinary Exploration and Research in Astrophysics (CIERA), Northwestern University, Evanston, IL 60202, USA
[20] ELTE Eötvös Loránd University, Gothard Astrophysical Observatory, Szent Imre herceg út 112, Szombathely 9700, Hungary
[21] Department of Physics, University of California, Berkeley, CA 94720, USA
[22] Graduate Institute of Astronomy, National Central University, 300 Zhongda Road, Zhongli, Taoyuan 32001, Taiwan
[23] ELTE Eötvös Loránd University, Institute of Physics and Astronomy, Pázmány Péter sétány 1/A, Budapest 1117, Hungary
[24] Institute of Astronomy and Kavli Institute for Cosmology, Madingley Road, Cambridge, CB3 0HA, UK
[25] Space Telescope Science Institute, Baltimore, MD 21218, USA
[26] Department of Physics and Astronomy, Northwestern University, Evanston, IL 60208, USA
[27] Thacher School, 5025 Thacher Road, Ojai, CA 93203, USA
[28] MTA-ELTE Lendület "Momentum" Milky Way Research Group, Hungary

Received 2023 August 24; revised 2024 March 13; accepted 2024 March 27; published 2024 September 9

Abstract

We present the photometric and spectroscopic evolution of SN 2022oqm, a nearby multipeaked hydrogen- and helium-weak calcium-rich transient (CaRT). SN 2022oqm was detected 13.1 kpc from its host galaxy, the face-on spiral galaxy NGC 5875. Extensive spectroscopic coverage reveals an early hot ($T \geqslant 40{,}000$ K) continuum and carbon features observed ∼1 day after discovery, SN Ic-like photospheric-phase spectra, and strong forbidden calcium emission starting 38 days after discovery. SN 2022oqm has a relatively high peak luminosity ($M_B = -17$ mag) for CaRTs, making it an outlier in the population. We determine that three power sources are necessary to explain the light curve (LC), with each corresponding to a distinct peak. The first peak is powered by an expanding blackbody with a power-law luminosity, suggesting shock cooling by circumstellar material (CSM). Subsequent LC evolution is powered by a double radioactive decay model, consistent with two sources of photons diffusing through optically thick ejecta. From the LC, we derive an ejecta mass and ^{56}Ni mass of $\sim 0.6\,M_\odot$ and $\sim 0.09\,M_\odot$. Spectroscopic modeling $\sim 0.6\,M_\odot$ of ejecta, and with well-mixed Fe-peak elements throughout. We discuss several physical origins for SN 2022oqm and find either a surprisingly massive white dwarf progenitor or a

---

[29] ISEF International Fellowship.

peculiar stripped envelope model could explain SN 2022oqm. A stripped envelope explosion inside a dense, hydrogen- and helium-poor CSM, akin to SNe Icn, but with a large 56Ni mass and small CSM mass could explain SN 2022oqm. Alternatively, helium detonation on an unexpectedly massive white dwarf could also explain SN 2022oqm.

Unified Astronomy Thesaurus concepts: White dwarf stars (1799); Binary stars (154); Supernovae (1668)

Materials only available in the online version of record: data behind figures, machine-readable tables

1. Introduction

Calcium-rich transients (CaRTs) are observationally rare. They tend to be fainter than most supernovae (typically $-16 \lesssim M_B \lesssim -15$ mag), show strong forbidden calcium and weaker forbidden oxygen emission during the nebular phase ([Ca II]/[O I] >2), and have a fast light curve (LC) rise time ($t_{\rm rise} \lesssim 15$ days) (Filippenko et al. 2003; Perets et al. 2010; Waldman et al. 2011; Kasliwal et al. 2012; Meng & Han 2015; De et al. 2020; Jacobson-Galán et al. 2022). In total, only 38 such transients have been identified in the literature. Although the rates of CaRTs are likely in the range of 5%–20% of the normal SNe Ia rates, the relatively dim peak magnitudes and quick LC evolution times make these supernovae (SNe) more difficult to detect than other types (Perets et al. 2010; Kasliwal et al. 2012; Meng & Han 2015; De et al. 2020; Zenati et al. 2023). As the set of well-observed CaRTs has grown, a rich diversity of observational characteristics has emerged.

CaRTs are typically found offset from their host galaxy, suggesting a predominantly older progenitor population (with some notable exceptions; see De et al. 2020 for a review). CaRTs are typically discovered in stellar clusters in elliptical galaxies (Perets et al. 2010; Kasliwal et al. 2012; Foley 2015; Jacobson-Galán et al. 2020a; De et al. 2020; Perets & Beniamini 2021; Zenati et al. 2023), consistent with this older population. However, some of the CaRTs, namely iPTF15eqv (Milisavljevic et al. 2017), iPTF16hgs (De et al. 2018a), SN 2016hnk (Galbany et al. 2019; Jacobson-Galán et al. 2020b), SN 2019ehk (Jacobson-Galán et al. 2020a), and SN 2021gno (Jacobson-Galán et al. 2022; Ertini et al. 2023) are located in spiral star-forming galaxies, with significant offsets from the closest star-forming regions within their host galaxies (Jacobson-Galán et al. 2022). Nevertheless, population studies of CaRTs (e.g., Shen et al. 2019) find that CaRT locations are generally consistent with populations of old ($\gtrsim$5 Gyr) and low-metallicity ($Z/Z_\odot \leqslant 0.3$) stars.

CaRTs are not the only class of SNe that have strong forbidden nebular calcium emission. Particularly, SNe Iax are known to have strong forbidden calcium emission (Silverman et al. 2012b; Siebert et al. 2020). However, these are likely distinct classes of transients as SNe Iax have longer-lived LCs (approximately years compared to approximately months) and bluer photospheric-phase spectra (Foley et al. 2013; Kawabata et al. 2021). In addition, CaRTs themselves have large spectroscopic diversity. Compared to other classes of SNe, De et al. (2020) find that some CaRTs are spectroscopically more similar to Type Ia SNe (Ia-like CaRTs; CaRTs-Ia), while others are more similar to Type Ibc SNe (Ibc-like CaRTs; CaRTs-Ibc). Furthermore, Das et al. (2022) presented a population of CaRTs-IIb, although they predicted a distinct progenitor for these transients. Such spectroscopic diversity points to the possibility that several distinct progenitor systems give rise to the observed population of CaRTs.

Although the progenitor nature of CaRTs remains elusive, Perets et al. (2010) proposed a theory to explain the prototypical CaRT SN 2005E: the detonation of a helium shell on the surface of a WD in a binary WD (BWD) system. Helium can be accreted onto a WD without detonating the WD from either an He-rich WD or from a nondegenerate He star (Holcomb et al. 2013; Shen et al. 2019). As He is accreted, the He shell can reach the critical density to ignite (Guillochon et al. 2010; Dan et al. 2012; Dessart & Hillier 2015). However, the burning of the He shell should not trigger a WD core detonation, which constrains the WD mass to $\leqslant 0.8\,M_\odot$. Therefore, a BWD system within this narrow region of parameter space could be a CaRT progenitor (Shen et al. 2010; Dan et al. 2011, 2012; Waldman et al. 2011; Shen et al. 2019; Jacobson-Galán et al. 2020a; De et al. 2020; Zenati et al. 2023). Indeed, Zenati et al. (2023) presented a similar scenario involving a BWD system consisting of a secondary carbon–oxygen WD (C/O WD) and a primary He+C/O hybrid WD, where the He envelope contains ~2%–20% of the primary WD's mass. Before the merger, the secondary WD is fully disrupted by the primary WD, causing CO from the secondary to accrete onto the primary and heat the He shell. An He-enriched detonation occurs in the primary, leading to a weak explosion and an intact core.

Here, we present observations of a recent CaRT-Ic, SN 2022oqm, in the nearby ($z = 0.012$) star-forming spiral galaxy NGC 5875. Upon discovery, SN 2022oqm was initially classified as an SN I (Zimmerman et al. 2022), given the absence of hydrogen and helium, and the lack of obvious silicon in its earliest spectrum. In addition, the peak magnitude of SN 2022oqm ($M_B = -17$) is typical of SNe Ic, further supporting the SN Ic classification. However, nebular phase spectroscopy reveals that SN 2022oqm is a CaRT, the 39th of its class (see Table 5), and among the brightest CaRTs-Ibc detected so far (Jacobson-Galán et al. 2020a; De et al. 2020; Das et al. 2022). Therefore, an important question emerges: Was SN 2022oqm the result of the core collapse of a massive star (core-collapse supernova, CCSN), the standard progenitor of SNe Ic, or was its progenitor a binary WD system? In this study, we address this and other peculiarities in the evolution of SN 2022oqm. Irani et al. (2022) also presents a detailed analysis of this event, focusing primarily on the first peak, and constraining the mass of the circumstellar material (CSM). In this article, we present a largely independent and complementary analysis of SN 2022oqm and find broad agreement with Irani et al. (2022). Where possible, we present comparisons to their work and show potential disagreements between the two analyzes.

In Section 2, we present our photometric and spectroscopic observations. In Section 3, we present the photometric analysis of SN 2022oqm. In Section 4, we present the full spectral sequence of SN 2022oqm, along with a detailed analysis of the spectra of SN 2022oqm. In Section 5, we present modeling of the LC of the SN 2022oqm. In Section 6, we compare SN 2022oqm to the

Table 1
SN 2022oqm and NGC 5875 (Host Galaxy) Properties

Parameter	Value	References
R.A.	$15^{\mathrm{h}}09^{\mathrm{m}}08\overset{\mathrm{s}}{.}21$	(2)
Decl.	$+52°32'05\overset{''}{.}14$	(2)
Redshift	0.012	(4)
Distance Modulus	33.575	(4)
Milky Way $E[B - V]$	0.016	(3)
Explosion Time	MJD = 59770–59771 2022 Jul 10–11	This Work
Time of Peak 1	MJD = 59771 2022 Jul 11	This Work
Time of Peak 2	MJD = 59775 2022 Jul 13–17	This Work
Time of Peak 3	MJD = 59785 2022 Jul 18–25	This Work
Host R.A.	$+15^{\mathrm{h}}09^{\mathrm{m}}13\overset{\mathrm{s}}{.}16$	(1)
Host decl.	$52°31'42\overset{''}{.}40$	(1)
Host-SN Offset	$50\overset{''}{.}6$ (13.1 kpc)	This Work

References. (1) Abazajian et al. (2005); (2) Sollerman et al. (2022); (3) Schlafly & Finkbeiner (2011); (4) van Driel et al. (2016).

broader CaRT population. In Section 7, we explore possible progenitor scenarios of SN 2022oqm. We discuss our results in Section 8 and conclude in Section 9. We assume a standard ΛCDM cosmology throughout ($H_0 = 67.8$ km s^{-1} Mpc^{-1}, Ω_M=0.31, $\Omega_\Lambda = 0.69$; Planck Collaboration et al. 2016).

2. Observations

SN 2022oqm was reported to the Transient Name Server with a discovery date of 2022 July 11 04:33 UT (MJD = 59771.69) and the last nondetection a day earlier on 2022 July 10 06:14 UT (MJD = 59770.75) by Sollerman et al. (2022), and initially classified as a SN I (Zimmerman et al. 2022). Immediately after detection, a clear shock-like UV excess had become apparent, and the community began to follow the evolution of SN 2022oqm. After discovery, SN 2022oqm was next classified as an SN Ic (D. Perley et al. 2022; Leadbeater 2022), and finally as an SN Ic-pec (Fulton et al. 2022). Its observed properties are summarized in Table 1. SN 2022oqm was found offset by $50\overset{''}{.}6$ (13.1 kpc) from the center of NGC 5875, an extended spiral galaxy at 53.5 ± 1 Mpc (Tully et al. 2013).

2.1. Photometry

A log of all photometry presented in this article is provided in Table 7.

2.1.1. Pan-STARRS

SN 2022oqm was observed with the Pan-STARRS telescope (PS1/2; Kaiser et al. 2002; Chambers et al. 2017) on 2022 September 8 in *rz* bands through the Young Supernova Experiment (YSE; Jones et al. 2021). Data storage/visualization and follow-up coordination was done through the YSE-PZ Target and Observation Manager (Coulter et al. 2022, 2023). The YSE photometric pipeline is based on `photpipe` (Rest et al. 2005), which relies on calibrations from Magnier et al. (2020) and Waters et al. (2020). Each image template was taken from stacked PS1 exposures, with most of the input data from the PS1 3π survey. All images and templates were resampled and astrometrically aligned to match a skycell in the PS1 sky tessellation. An image zero point is determined by comparing point-spread-function (PSF) photometry of the stars to updated stellar catalogs of PS1 observations (Flewelling et al. 2020). The PS1 templates are convolved with a three-Gaussian kernel to match the PSF of the nightly images, and the convolved templates are subtracted from the nightly images with `HOTPANTS` (Becker 2015). Finally, a flux-weighted centroid is found for the position of the SN in each image and PSF photometry is performed using "forced photometry": the centroid of the PSF is forced to be at the SN position. The nightly zero point is applied to the photometry to determine the brightness of the SN for that epoch.

2.1.2. Las Cumbres Observatory Global Supernova Experiment

The Las Cumbres Observatory (LCO) triggered observations through the Global Supernova Experiment on SN 2022oqm within two weeks prior to the peak. Observations were conducted by the Sinistro 1 m telescopes from Las Cumbres Observatory. Data were recorded in the *B*, *g*, *V*, *r*, and *i* bands covering 11 days prepeak and 52 days postpeak. We reduced the photometry in house using the `lcogtsnpipe`[30] infrastructure (Valenti et al. 2016), which uses the PSF fitting procedure to extract target magnitudes. We calibrated photometry in the *B* and *V* bands using Vega magnitudes in the Landolt catalog (Landolt 1992). We calibrated photometry in the *g*, *r*, and *i* bands to AB magnitudes using the Sloan Digital Sky Survey (SDSS) catalog (Smith et al. 2002).

2.1.3. Thacher, Lulin, LCO, Nickel

We observed SN 2022oqm with the Thacher 0.7 m telescope (Swift et al. 2022) in *griz* bands from 2022 July 12 to September 9, with the Lulin 1 m telescope in *griz* bands from 2022 August 9 to 30, and with the LCO 1 m telescopes and Sinistro imagers in *ugri* bands from 2022 August 2 to 10. All images were reduced in `photpipe` (Rest et al. 2005) with bias, flat, and dark frames obtained in the same instrumental configuration as our science images. We regridded each frame to a common pixel scale and field center with `SWarp` (Bertin 2010) and performed point-spread function photometry with a custom version of `DoPhot` (Schechter et al. 1993). All photometry was calibrated using standard stars from the PS1 3π DR2 catalog (Flewelling et al. 2020) observed in the same field as SN 2022oqm. We subtracted pre-explosion *griz* template images from PS1 using `hotpants` (Becker 2015) and performed forced photometry at the site of SN 2022oqm in the subtracted images, which is the final photometry presented here.

2.1.4. Konkoly, Baja Observatories

Photometric observations of SN 2022oqm were collected from Piszkesteto Station of Konkoly Observatory and from Baja Observatory of University of Szeged, Hungary. Both sites are equipped with a robotic 0.8 m Ritchey–Chretien–Nasmyth telescope, manufactured by ASA AstroSysteme GmbH, Austria. Photometry was performed by applying a back-illuminated, liquid-cooled, 2048 × 2048 FLI ProLine PL230 CCD camera through Johnson *B*, *V*, and Sloan g', r', i' and z' bands. Image reductions were done by custom-made IRAF[31] and `fitsh`[32] scripts. Photometry of the SN was calibrated via

---

[30] https://github.com/LCOGT/lcogtsnpipe

[31] https://iraf-community.github.io/

[32] https://fitsh.net/

local point sources within the CCD field-of-view using their PS1 photometry.[33]

2.1.5. Asteroid Terrestrial-impact Last Alert System (ATLAS)

SN 2022oqm was detected in the *c* and *o* bands by ATLAS between −20 and 70 days relative to the phase of *r*-band peak. Using the ATClean toolkit (Rest et al. 2023), we searched for any explosion activity by running a Gaussian-weighted rolling sum on the flux/dflux of the pre-SN LC to compare to the control light curves close to the SN position. The pre-SN rolling sum was within the noise of the control light curve sums suggesting no evidence for any pre-SN bumps in the ATLAS LC data. We used the ATLAS forced-photometry server (Tonry et al. 2018; Smith et al. 2020; Shingles et al. 2021) to recover the difference-image photometry for SN 2022oqm. To remove erroneous measurements and have significant SN flux detection at the location of SN 2022oqm, we applied several cuts on the total number of individual data points and nightly averaged data. Our first cut used the χ^2 and uncertainty values of the PSF fitting to remove discrepant data. We then obtained forced photometry of eight control LCs located in a circular pattern around the location of the SN with a radius of 17″. The flux of these control LCs is expected to be consistent with zero, and any significant deviation from zero would indicate that there are either unaccounted systematic biases or underestimated uncertainties. We searched for such deviations by calculating the weighted mean of the set of control light-curve measurements for a given epoch after removing any $>3\sigma$ outliers (for a more detailed discussion, Rest et al. 2023.)[34] If the weighted mean of these photometric measurements was inconsistent with zero, we flagged and removed those epochs from the SN LC. This method allows us to identify potentially incorrect measurements without using the SN LC itself. We then binned the SN 2022oqm LC by calculating a 3σ-cut weighted mean for each night (ATLAS typically has four epochs per night), excluding the flagged measurements from the previous step.

2.1.6. ZTF

We retrieved photometry of SN 2022oqm from the Zwicky Transient Facility (ZTF) public survey in ZTF-*g* and ZTF-*r* bands (see Bellm et al. 2019, for details). Following the methodology in Aleo et al. (2023), we used forced photometry of SN 2022oqm in ZTF difference imaging from the Las Cumbres Observatory's Make Alerts Really Simple public alerts broker Fink (Möller et al. 2021).

2.1.7. Swift

SN 2022oqm was observed with the Ultraviolet Optical Telescope (UVOT; Roming et al. 2005) onboard the Neil Gehrels Swift Observatory (Gehrels et al. 2004) from 2022 July 11 until 2022 July 29. We performed aperture photometry with a 5″ region with `uvotsource` within HEAsoft v6.26,[35] following the standard guidelines from Brown et al. (2014). In order to remove contamination from the host galaxy, we employed images acquired at $t \approx 122$ days after the explosion, assuming that the SN contribution is negligible at this phase. This is supported by visual inspection in which we found no flux associated with SN 2022oqm. We subtracted the measured background count rate at the location of the SN from the count rates in the SN images following the prescriptions of Brown et al. (2014). Consequently, we detect bright UV emission from the SN directly after the explosion until maximum bolometric light. Subsequent non-detections in *w*1, *m*2, and *w*2 bands indicate significant cooling of the photosphere and/or Fe-group line blanketing.

Observed contemporaneously with the UVOT, Swift also observed SN 2022oqm using the X-Ray Telescope (XRT; Burrows et al. 2005) in photon-counting mode. Using the most up to date calibrations and the standard filters and screenings, all level 1 XRT observations were processed using the XRTPIPELINE version 0.13.7. Using a region with a radius of 47″ centered on the location of SN 2022oqm and a source free background region, we found no X-ray emission coincident with the location of SN 2022oqm. To place the deepest constraints on the presence of X-ray emission, we merged all available Swift observations of SN 2022oqm using the HEASOFT tool XSELECT version 2.5b. We then derived a 3σ upper limit to the absorbed flux in the 0.3–10.0 keV energy range of 6.79×10^{-14} erg cm s^{-1}, assuming an absorbed power law with a column density of 1.73×10^{20} cm^{-2} (HI4PI Collaboration et al. 2016) and a photon index of 2 that is redshifted to the location of SN 2022oqm's host galaxy.

2.2. Spectroscopy

A log of all spectra presented in this article is provided in Table 6.

2.2.1. Hobby Eberly Telescope

Six optical spectra were taken through the Low-Resolution Spectrograph 2 (LRS2) instrument on the Hobby Eberly Telescope (HET) on 2022 July 13, 16, 17, 24, and 30 and 2022 August 2. The LRS2 data were processed with `Panacea`,[36] the HET automated reduction pipeline for LRS2. The initial processing includes bias correction, wavelength calibration, fiber-trace evaluation, fiber normalization, and fiber extraction; moreover, there is an initial flux calibration from default response curves, an estimation of the mirror illumination, as well as the exposure throughput from guider images. After the initial reduction, we used an advanced code designed for crowded IFU fields to perform a careful sky subtraction and host-galaxy subtraction. Finally, we modeled the target SNe with a Moffat (1969) PSF model and performed a weighted spectral extraction.

2.2.2. Kast and LRIS

Seven optical spectra were taken with the Kast dual-beam spectrograph (Miller & Stone 1993) on the Shane 3 m telescope at Lick Observatory, on 2022 July 19, 24, and 28 and 2022 August 2, 7, 13, and 17. One spectrum was taken with the Low-Resolution Imaging Spectrograph (LRIS; Oke et al. 1995) on the 10 m Keck I telescope on the 2022 September 25. To reduce the Kast and LRIS spectral data, we used the `UCSC Spectral Pipeline`[37] (Siebert et al. 2019), a custom data-reduction pipeline based on procedures outlined by Foley et al.

---

[33] https://catalogs.mast.stsci.edu/panstarrs/

[34] https://github.com/srest2021/atlaslc

[35] We used the calibration database (CALDB) version 20201008.

[36] https://github.com/grzeimann/Panacea

[37] https://github.com/msiebert1/UCSC_spectral_pipeline

(2003), Silverman et al. (2012a), and references therein. The two-dimensional spectra were bias-corrected, flat-field corrected, adjusted for varying gains across different chips and amplifiers, and trimmed. Cosmic-ray rejection was applied using the `pzapspec` algorithm to individual frames. Multiple frames were then combined with appropriate masking. One-dimensional spectra were extracted using the optimal algorithm (Horne 1986). The spectra were wavelength calibrated using internal comparison-lamp spectra with linear shifts applied by cross-correlating the observed night-sky lines in each spectrum to a master night-sky spectrum. Flux calibration was performed using standard stars at a similar airmass to that of the science exposures, with "blue" (hot subdwarfs; i.e., sdO) and "red" (low-metallicity G/F) standard stars. We correct for atmospheric extinction. By fitting the continuum of the flux-calibrated standard stars, we determine the telluric absorption in those stars and apply a correction, adopting the relative airmass between the standard star and the science image to determine the relative strength of the absorption. We allow for slight shifts in the telluric A and B bands, which we determine through cross-correlation. For dual-beam spectrographs, we combine the sides by scaling one spectrum to match the flux of the other in the overlap region and use their error spectra to correctly weight the spectra when combined. More details of this process are discussed elsewhere (Foley et al. 2003; Silverman et al. 2012a; Siebert et al. 2019).

2.2.3. NIRES

We obtained a near-infrared (NIR; 0.94–2.45 μm) spectrum of SN 2022oqm using the Near-Infrared Echellette Spectrometer (NIRES; Wilson et al. 2004) on the 10 m Keck II telescope as part of the Keck Infrared Transient Survey (KITS), a NASA Keck Key Strategic Mission Support program (PI R. Foley). We observed the SN at two positions along the slit (AB pairs) to perform background subtraction. An A0V star was observed immediately before or after the science observation. We reduced the NIRES data using `spextool v.5.0.2` (Cushing et al. 2004); the pipeline performs flat-field corrections using observations of a standard lamp and wavelength calibration based on night-sky lines in the science data. We performed telluric correction using `xtellcor` (Vacca et al. 2003).

2.2.4. ALFOSC

One spectrum was taken with the Alhambra Faint Object Spectrograph and Camera (ALFOSC) on the Nordic Optical Telescope (NOT) at La Palma on the 15th of July 2022. This spectrum was taken using grism 4 and a 1.000 slit, aligned along the parallactic angle, and under clear observing conditions and good seeing. It was reduced with a custom pipeline running standard `pyraf` procedures.

2.2.5. Las Cumbres Observatory Global Supernova Experiment

Two spectra were obtained by the Faulkes Telescope North with the FLOYDS low-resolution spectrograph on 2022 August 12 and 19. These data were reduced via the pipeline as detailed in Valenti et al. (2013).

3. Photometric Analysis

SN 2022oqm was discovered in the outskirts of a face-on, spiral galaxy, NGC 5875, shown in Figure 1. Like most CaRTs, SN 2022oqm is highly offset from the center of the galaxy. The host redshift is consistent with SN 2022oqm, showing SN 2022oqm is not a chance coincidence with the galaxy's location. SN 2022oqm is visibly offset from any ongoing star formation. To quantify the radial offset of SN 2022oqm in terms of the host light, we adopt a fractional light method previously employed in SN environmental studies (e.g., Fruchter et al. 2006; Habergham et al. 2014; Ransome et al. 2022). In the case of SN 2022oqm, we use g-band imaging from a Pan-STARRS PS1 pre-explosion image of the galaxy. This technique uses ellipses in the same "aspect ratio" as the galaxy (position angle and axis ratio from NED[38] with an axis ratio of ~2.5). An ellipse that is gradually expanded until the difference between iterations becomes small (i.e., consistent with reaching the background) is the host ellipse. Another ellipse with the same aspect ratio that intercepts the SN location is the SN ellipse. The total light emitted inside the SN ellipse is divided by the total light emitted inside the host ellipse, giving the fractional light enclosed by the SN, which is 96% for SN 2022oqm. We also calculate that the location of SN 2022oqm is ~2.4 half-light radii from the center of the galaxy. Using Pan-Starrs PS1 pre-explosion imaging of the galaxy, we find no indication of pre-explosion flux at the position of the transient, to a limiting surface brightness 24.5 mag arcsec^{-2}. The two closest clusters of optical light are 11.″2 (2.9 kpc) and 13.″6 (3.5 kpc) away.

Photometry reveals SN 2022oqm is a multipeaked SN. Our near-infrared to ultraviolet LC of SN 2022oqm is shown in Figure 2. We detected an early peak that is more pronounced in shorter wavelengths at the time of detection (MJD 59771.19). There is another, broader peak between MJD ~59781 and ~59788. We also note a weak local maximum of the U-band flux at MJD 59774.24 (see Section 5.3 for a detailed discussion on the confirmation and origin of these three peaks). We note the approximate phases of these three as peaks 1, 2, and 3 in Figure 2. We report phase relative to the time of maximum r-band flux (MJD 59784.17) and present epochs with respect to this phase henceforth in this article. The peak luminosity of SN 2022oqm is in the typical range of peak SN Ibc luminosities (−17 to −18 mag; Drout et al. 2011), but is ~1.5 mag brighter than the population of CaRTs-Ibc at peak (De et al. 2020; Zenati et al. 2023).

In Figure 3, we show $B-V$ (top) and $r-i$ (bottom) color evolution of SN 2022oqm with known CaRTs, the well-studied SN Ib with evidence of a binary progenitor iPTF13bvn (Cao et al. 2013; Bersten et al. 2014), and a template SN Ia LC. We use the canonical $s=1$ model from Nugent et al. (2002) to find a template SN Ia LC (see Section 6 for a more detailed description of this model). We also show the three theoretical models of differing progenitor scenarios that result in CaRTs from Zenati et al. (2023): fca1, fca2, and fca3. The $r-i$ color evolution of SN 2022oqm matches that of other CaRTs but the $B-V$ color evolution for SN 2022oqm matches that of SNe Ia and SNe Ibc. The $B-V$ color of SN 2022oqm is bluer than that of most CaRTs. The tracks of *fac1*, *fca2*, and *fca3* predict redder colors than what is seen in SN 2022oqm (see Section 7 for a detailed description of this progenitor system).

---

[38] https://ned.ipac.caltech.edu/

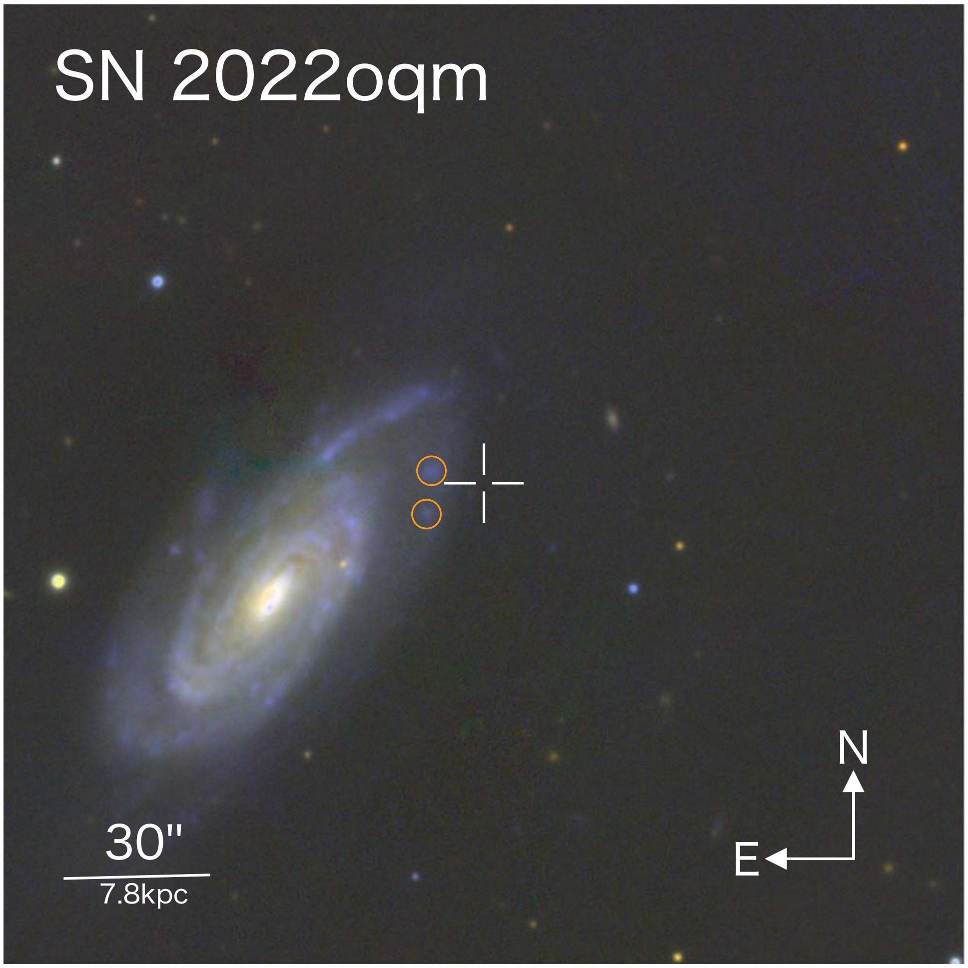

Figure 1. Pan-STARRS image the host galaxy NGC5875, at ($15^{\mathrm{h}}09^{\mathrm{m}}10\overset{\mathrm{s}}{.}31$, $52^\circ32'19\overset{''}{.}72$). We indicate the location of SN 2022oqm in the white crosshairs. The closest knots of star formation (marked in orange) are 2.9 and 3.5 kpc away.

3.1. Bolometric Properties

We use the `extrabol` (Thornton & Villar 2022) package to estimate the bolometric luminosity (L_{bol}), blackbody temperature (T), and photosphere radius (R_{phot}) of SN 2022oqm over time. The `extrabol` package interpolates the LC in each band using a Gaussian process with a two-dimensional 3/2-Matern kernel, accounting for correlation in both time and wavelength. A blackbody spectral energy distribution (SED) is then fit to each observed epoch, inferring bolometric luminosities, blackbody radii, and blackbody temperatures with time. The fitted L_{bol}, T, and R_{phot} are shown in Figure 4, while the bolometric luminosity, temperature, and radius during peaks 1, 2, and 3 are listed in Table 2.

At the time of detection, SN 2022oqm is very hot ($T \approx 40{,}000$ K), rapidly expanding, and cooling between peak 1 (first detection) to peak 2, where the temperature decreases by a factor of 5 and the bolometric luminosity decreases by a factor of 10. After peak 2, the object continues to cool down and expand, but the bolometric luminosity increases by a factor 1.5 until peak 3. By integrating the bolometric luminosity over all time, we find at 1σ significance, the total energy emitted ranges from $48.6 \leqslant \log_{10}[E_{\mathrm{tot}}/\mathrm{erg}] \leqslant 49.1$. We find our derived blackbody luminosity and temperatures are within 1σ of the derived values in Irani et al. (2022).

4. Spectroscopic Analysis

We present 22 spectra that were taken between $t = -14$ days and $t = 62$ days in Figures 5, 6, and 7. The earliest spectrum (-12.86 days) is publicly available and was presented by Zimmerman et al. (2022) to obtain the earliest classification of SN 2022oqm. This spectrum is dominated by a blue continuum with a C IV emission feature at 5805 Å and N III at 4638 Å. Irani et al. (2022) present multiple spectra with a higher signal-to-noise ratio at this phase, identifying the same emission features in addition to strong O III, O IV, and O V features. The presence of such high ionization levels suggests the presence of an intense UV radiation field (Quimby et al. 2007; Leloudas et al. 2019). Indeed fitting a blackbody curve to the earliest spectrum suggests a temperature in excess of 3×10^4 K, in agreement with our photometrically inferred earliest temperature (see Figure 4). The observed narrow highly ionized species during the earliest phase of SN 2022oqm points to the presence of CSM in the system, where nonthermal photons are being created by the interaction between the SN ejecta and CSM. After shock breakout, the excited CSM cools through shock cooling, powering the earliest phase of the LC. The earliest spectrum suggests that the CSM lacks H and He, although C and O are observed.

We observe the Ca II H&K complex at 3933 Å, the Mg II λ4481 feature, a weak S II λ6355 absorption line, a weak C II

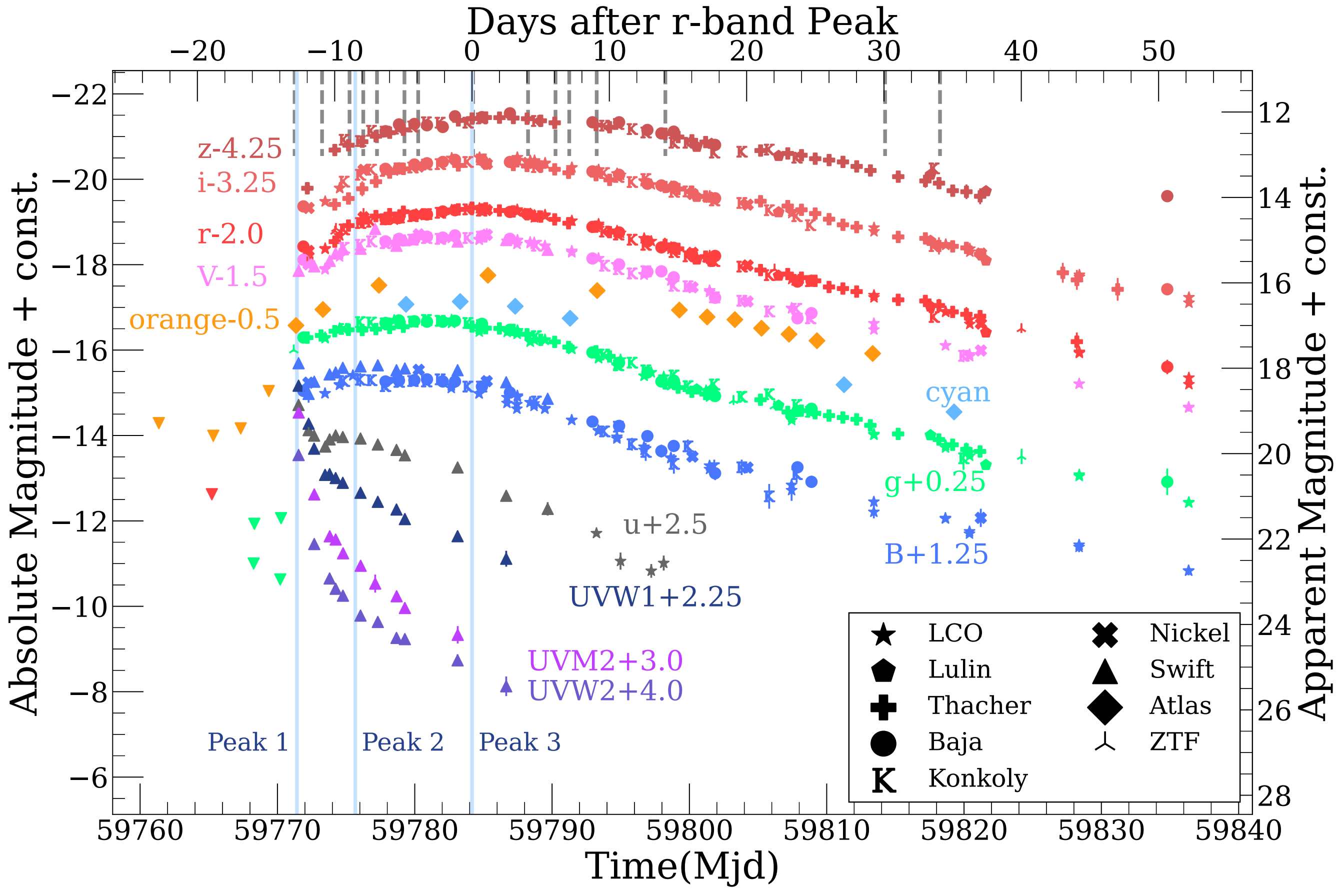

Figure 2. Multiband light curve of SN 2022oqm. Dotted gray vertical lines represent epochs where we obtain spectroscopy. Phases of peaks 1, 2, and 3 are labeled with blue vertical lines. Upper limits (3σ) are identified as downward-facing triangles. Photometry in the *B* filter appears to be scattered because the swift *B*-filter bandpass is slightly different from the bandpass of the *B* filter on other instruments. The precise shape of the bandpass is accounted for in photometric analysis presented throughout. The multiband apparent AB photometry is available as the data behind the figure.

(The data used to create this figure are available in the online article.)

λ6580 absorption line, and an O I λ7775 feature before peak 3. The NIR spectrum taken on $t = -6$ days (Figure 7) shows no clear evidence of helium, unlike many CaRTs (see Section 6 for a detailed comparison between SN 2022oqm and CaRT spectroscopic signatures).

By $t \approx 30$ days, we find the SN has begun transitioning to its nebular phase, revealing significant forbidden line emission. By this time, a clear [Ca II] $\lambda\lambda$7291, 7324 emission feature becomes apparent. Using the most recently available spectrum ($t = 62$ days), in which SN 2022oqm approaches the nebular phase, we attempt to measure an emission flux ratio [Ca II] $\lambda\lambda$7291, 7324/[O I] $\lambda\lambda$6300, 6364. Because [O I] emission is not clearly detected, we measure the total flux within the equivalent width of the [Ca II] $\lambda\lambda$7291, 7324 line centered at the [O I] $\lambda\lambda$6300, 6364 line location. We place a lower limit of $\approx$4.4, greater than the defined cutoff of 2 to be considered a CaRT (Perets et al. 2010; De et al. 2020; Jacobson-Galán et al. 2022).

We also plot the spectra of the He-rich CaRT SN 2021gno studied in detail by Jacobson-Galán et al. (2022) and Ertini et al. (2023) in Figures 5 and 6. We show the phase of the SN 2021gno spectra with respect to the epoch of *r*-band peak of SN 2021gno, facilitating easy comparison between the phases of SN 2021gno and SN 2022oqm. We find that with the exception of the highly ionized line transitions found in the earliest spectrum of SN 2022oqm and the He I λ5876 feature in SN 2021gno, all lines found in the spectra of SN 2022oqm are also found in those of SN 2021gno. This broad agreement with both spectral sequences further supports the CaRT classification of SN 2022oqm. We compare photospheric and nebular spectra of SN 2022oqm to those of SN 2021gno in more detail in Section 4.2.

Spectroscopic observations enable a census of elemental abundance, density, and velocity structures within the SN ejecta. As the ejecta expand, optical depth decreases with time, and the photosphere recedes into deeper layers of the ejecta. By measuring the line velocity of several elements over time, one can probe the velocity gradient of the ejecta. We present the velocities of O I λ7775, Si II λ6355, and Ca II H&K absorption lines during the photospheric phase of the SN in Figure 8. O I λ7775 velocity is roughly constant at $\sim$8000 km s^{-1} during the $\sim$20 days when this line is visible. Si II λ6355 declines in velocity, starting from $\sim$5000 km s^{-1} and reaching 3000 km s^{-1}. At early times, we observe Ca II H&K at $\sim$13,000 km s^{-1} and then approaches the O I λ7775 velocity from the time of peak 2 until immediately after peak 3. The times of peaks 1, 2, and 3 are highlighted with gray vertical lines. These velocities are typical for CaRTs and SNe Ic (Modjaz et al. 2016; De et al. 2020).

4.1. Spectral Synthesis Analysis

We model the observed spectral series of SN 2022oqm using `TARDIS` (Kerzendorf & Sim 2014), a one-dimensional Monte-

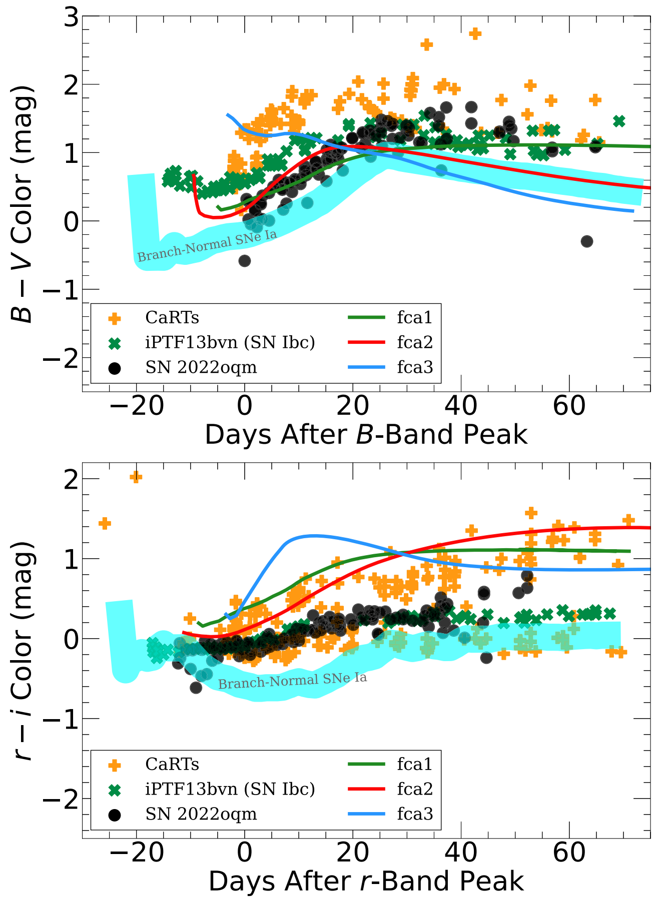

Figure 3. $B-V$ (top) and $r-i$ (bottom) color evolution of SN 2022oqm, compared to that of all CaRTs with well-sampled light curves, iPTF13bvn, the well-studied SN Ib with evidence of a binary progenitor, and the template of Branch-normal SNe Ia. SN 2022oqm is bluer than most CaRTs in both $r-i$ color and $B-V$ color. The three BWD models simulated by Zenati et al. (2023) are shown as *fca*1, *fca*2, and *fca*3. The SN 2022oqm color evolution is available as the data behind the figure.

(The data used to create this figure are available in the online article.)

Carlo radiative transfer code that numerically solves the radiative transport equation and models the spectral emission of SN ejecta. `TARDIS` treats photon-atom line interactions using a macroatom formalism, where the "macroatom" is the combination of the photon and atom. The macroatom formalism prescribes how the excited atom eventually de-excites and emits a photon and is explained in detail by Lucy (2002). `TARDIS` also assumes local thermodynamic equilibrium to simplify modeling the photon-atom interactions. In order to model helium, we have used the `recomb-nlte` treatment, which considers He I excited states as if they are in local thermodynamic equilibrium with higher ionization He II (see, e.g., Boyle et al. 2017).

By assuming homologous expansion of ejecta, `TARDIS` can parameterize ejecta layers by velocity. `TARDIS` takes ejecta density distribution, elemental abundance distribution, bolometric luminosity, and time since explosion as input to simulate an instantaneous SN spectrum produced by a prescribed range of velocities within the ejecta.

The CO21 model (Iwamoto et al. 1994) and the W7 Branch model (Nomoto et al. 1984; Branch et al. 1985) are the canonical density profiles in `TARDIS` for stripped-envelope

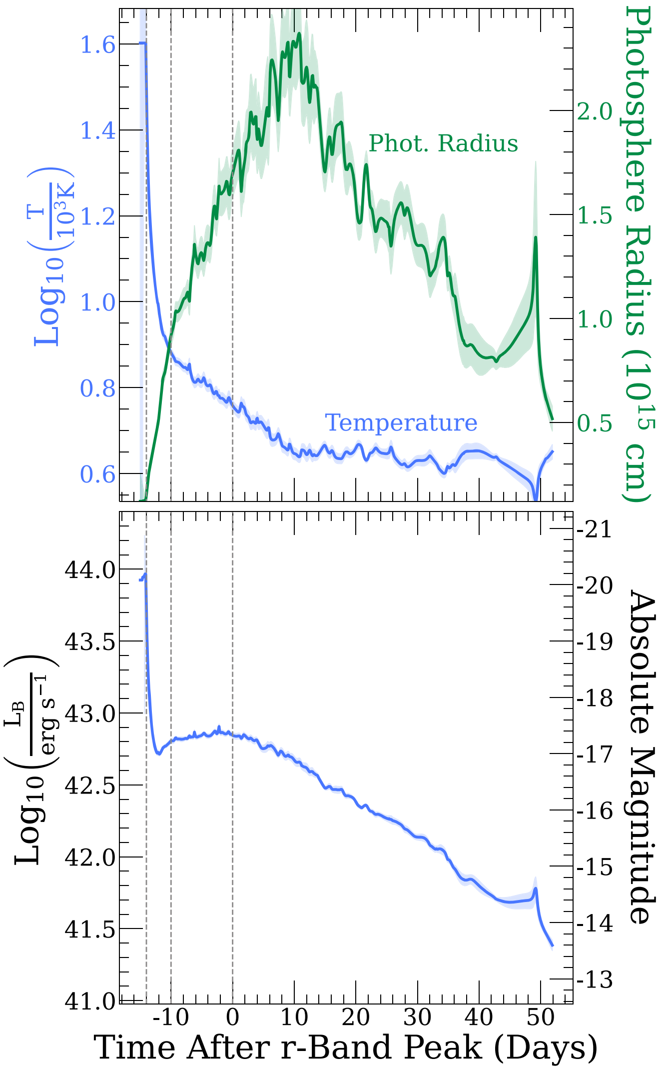

Figure 4. Blackbody fits to the photometry of SN 2022oqm, showing temperature and photosphere radius (top); and bolometric luminosity (bottom) evolution. Derived values at peaks 1, 2, and 3 are shown in gray. Numerical values are tabulated in text (see Section 3.1). The blackbody fits to the photometry of SN 2022oqm are available as the data behind the figure.

(The data used to create this figure are available in the online article.)

and thermonuclear explosions, respectively. We find that neither of these models reproduces the SN 2022oqm spectra well. As such, we utilize an exponential ejecta density profile to adequately fit the spectral sequence of SN 2022oqm. These three density profiles are reproduced in Figure 9. The exponential density profile mimics the Ic-like outer ejecta profile throughout the ejecta. The exponential density profile is constructed as $\rho \propto \exp\left(\frac{-3v}{10^4\ \mathrm{km\ s^{-1}}}\right)$ and has an integrated mass of $M_{\mathrm{ej}} = 0.57\,M_\odot$. The agreement to an exponential density profile is reminiscent of a disk-like ejecta structure (i.e., an alpha-disk model), but here we are limited to a one-dimensional geometry and therefore do not truly probe the angular distribution of the ejecta.

We fit four optical spectra at $t = -7.86$, -3.22, 0.07, and 4.08 days and one NIR spectrum at $t = -4.9$ days. Each simulation fits the velocity range and abundance of He, C, O, Ne, Si, Ca, and Fe-peak elements (including Ni and Co). We present atomic abundances that are denegerate in our modeling in the same category (e.g., Ne and O as "Ne+O" and Ni and Co

Table 2
Summary of Blackbody Properties of All Three Peaks as Derived from Fitting a Single Blackbody Evolution to the SN 2022oqm Light Curve with `extrabol`

Parameter	Peak 1	Peak 2	Peak 3
Temperature (K)	32,000 ± 3200	7600 ± 170	5700 ± 170
Photosphere Radius (cm)	$(1.5 \pm 0.14) \times 10^{14}$	$(9.2 \pm 0.49) \times 10^{14}$	$(1.7 \pm 0.12) \times 10^{15}$
Bol. Luminosity (erg s^{-1})	$(1.5 \pm 0.39) \times 10^{43}$	$(2.0 \pm 0.08) \times 10^{42}$	$(2.2 \pm 0.1) \times 10^{42}$
Bol. Magnitude	−19.4 ± 0.56	−17.1 ± 0.09	−17.2 ± 0.11

Note. Reported errors only account for statistical uncertainties.

as "Ni+Co"). We assume these elements are uniformly distributed through the velocity range fitted by each spectral fit. We show the fitted spectra in Figure 10 and the abundance distributions for each element in Figure 11. We find a general agreement between the simulated and the observed spectra, where the majority of spectral features are well reproduced. Some specific features, such as the broad absorption around 5200 Å at peak 3 are not correctly reproduced, likely due to a different ionization level of the line responsible for that absorption. We find a total ejecta mass of $\sim 0.6\, M_{\odot}$.

The resulting abundance pattern is characterized by (1) a predominant ejecta composition with a homogeneous distribution of both light elements (He, C, O, and Ne) and Fe-peak elements (Fe, Co, and Ni) and (2) a low Ca abundance at velocities $v_{\rm ej} \gtrsim 7900\ {\rm km\ s^{-1}}$, rapidly increasing when the most inner regions of the ejecta become visible at late epochs, e.g., days after peak brightness. The roughly uniform distribution of both Fe-peak and Ni+Co abundances throughout the ejecta shows agreement with the ^{56}Ni mixing and double-decay model suggested in Sections 5.4. A more detailed analysis of the iron features in the spectra could elucidate this, but such analysis is beyond the scope of this article. The enhancement of Ca during later spectra is consistent with the broadening of the later Ca lines observed ∼30 days after peak. A lack of distinct O and Ne features in our optical spectra mean that we are unable to constrain the individual abundance of either O or Ne.

Detailed spectroscopic modeling suggests a low He abundance in the ejecta of SN 2022oqm. Through `TARDIS` modeling, we find a helium mass upper limit of $8.43 \times 10^{-3}\, M_{\odot}$, corresponding to a mass fraction of ∼1.5% (see Figure 11). In addition, the commonly used He I λ10830 and He I λ20581 features are nonexistent in the NIR spectrum of SN 2022oqm (see Figure 7). A possible absorption feature is present near the He I λ10830 line, but it has been shown that this could be a blend of Mg (Filippenko et al. 1995; Williamson et al. 2021). Williamson et al. (2021) show that the He I λ20581 can be used to unambiguously constrain the presence of He because it is relatively separate from nearby lines. Moreover, Williamson et al. (2021) show that if He is present in considerable amounts in the system, the He I λ20581 will be visible. This feature is not detected in the NIR spectrum of SN 2022oqm, strongly suggesting a low abundance of He (see Figure 7). In Figure 7, we compare the NIR spectrum of SN 2022oqm to that of the He-poor SN Ic SN 2004aw (Taubenberger et al. 2006) and the He-rich SN Ib SN 2008D (Modjaz et al. 2009). SN 2008D has a clear He I λ20581 absorption line, revealing the presence of He in SN 2008D, whereas SN 2004aw and SN 2022oqm both do not have a clear detection of the He I λ20581 absorption line, suggesting a paucity of He (see Taubenberger et al. 2006 for a more detailed exploration of the presence of He in the spectrum of SN 2004aw).

4.2. Comparing SN 2022oqm to Other Transients

We overlay the spectrum of SN 2022oqm with those of SN 2007gr (a SN Ic, Valenti et al. 2008; Hunter et al. 2009), SN 2021gno (a CaRT, Jacobson-Galán et al. 2022; Ertini et al. 2023), and SN 2012Z (a SN Iax, Stritzinger et al. 2015; McCully et al. 2022) at peak (Figure 12) and during their nebular phases (Figure 13). At peak, we show Ca II $\lambda\lambda$3933 and 3968, Si II λ6347, and O I λ7775 with vertical lines, while for the nebular phase (Figure 13), we show the [O I] $\lambda\lambda$6300, 6364, [Ca II] $\lambda\lambda$7291, 7324, and Ca II $\lambda\lambda$8498, 8542, and 8662 with vertical lines. During the photospheric phase of SN 2022oqm, the spectrum closely resembles that of an SN Ic, where the strengths of calcium, silicon, and oxygen appear to be almost identical. The only inconsistency appears to be at shorter wavelengths, where line blanketing reduces flux more strongly in CaRTs than in SNe Ic. We also note that helium is clearly detected in at least some CaRTs but not in SN 2022oqm or the SN Ic. In the nebular phase, however, SN 2022oqm has a very different spectrum from that of the SN Ic. During the nebular phase, SNe Ic spectra feature a strong [O I] $\lambda\lambda$6300, 6364 emission line (Gaskell et al. 1986; Shivvers et al. 2019). This line is not detected in the spectrum of SN 2022oqm, which instead has a very strong [Ca II] $\lambda\lambda$7291, 7324 emission line, characteristic of CaRTs.

5. Detailed Light-curve Modeling

In this section, we model the LC of SN 2022oqm using several potential underlying power sources through the Modular Open-source Fitter for Transients (`MOSFiT`, Guillochon et al. 2018). `MOSFiT` is an open-source software that self-consistently models the time-variable SED following the framework originally presented in Arnett (1982). For each fit, we present goodness of fit through the Watanabe Akaike Information Criterion (WAIC) score, where a higher score represents a better fit to the data. The WAIC score accounts for parameter size by punishing models with more parameters (see Guillochon et al. 2018). Therefore, the WAIC score presents a method of comparing models with different parameter numbers and avoids the problem of overfitting. A WAIC score increase of at least 10 implies a significantly better model fit (Watanabe 2013; Gelman et al. 2014). We also measure goodness of fit for each model with the reduced chi-squared ($\chi^2_{\rm red}$) term.

The early excess in the LC seen in peak 1 (see Figure 2) is reminiscent of shock cooling following breakout of an SN shockwave out of surrounding CSM (see, e.g., Smith 2017; Piro et al. 2021). Following this peak, the behavior of the SN near peak 3 is similar to the more classical SN LC, which is powered by the radioactive decay of ^{56}Ni diffused through optically thick ejecta (Arnett 1982; Chatzopoulos et al. 2012). Within this framework, the ejecta mass ($m_{\rm ej}$), ejecta velocity ($v_{\rm ej}$), and gray-body opacity (κ) are fully degenerate, as all three primarily impact the overall diffusion timescale of the

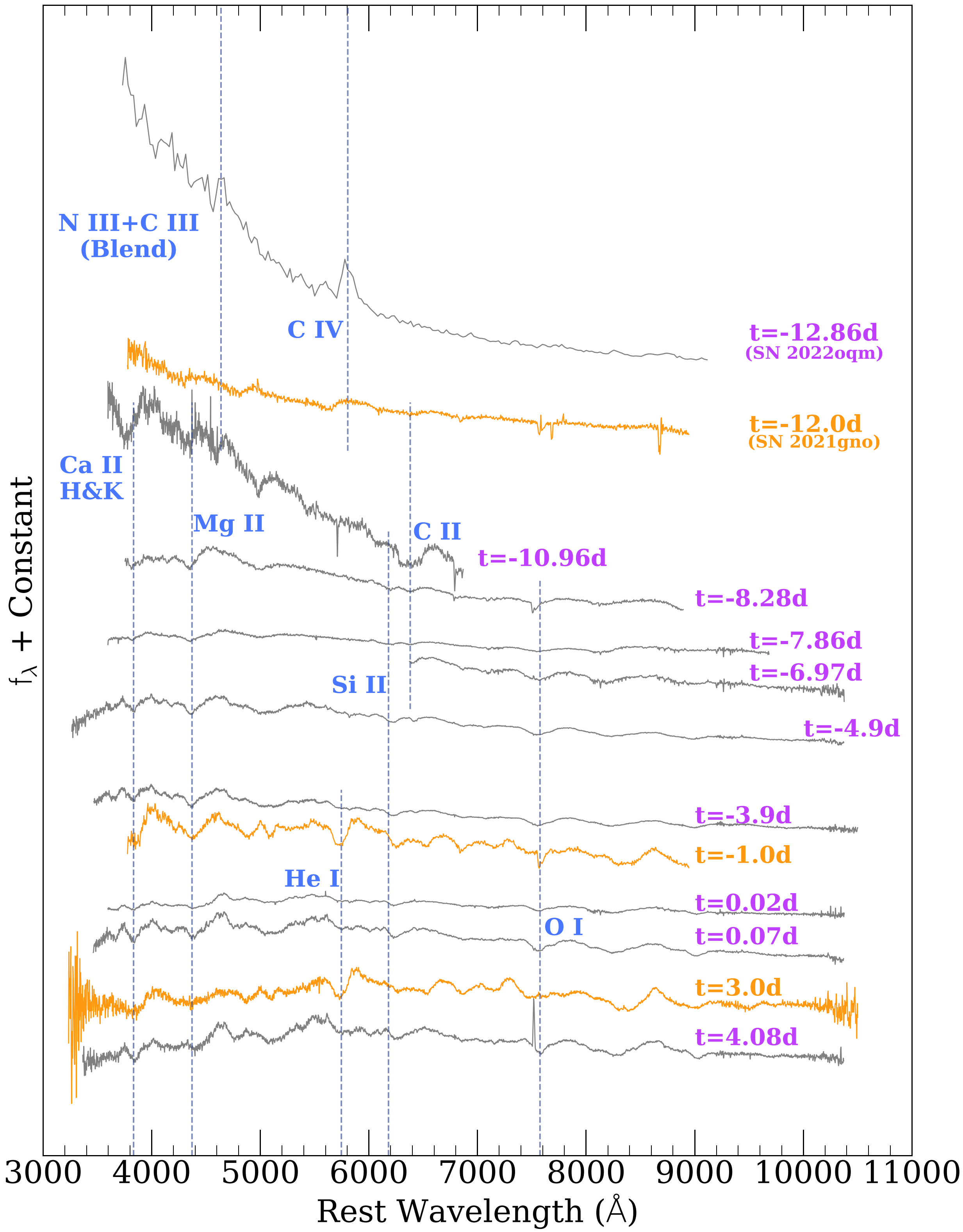

Figure 5. Spectral sequence of SN 2022oqm during −13 days ⩽ t ⩽ 5 days (gray) overlaid with the same-phase spectra of SN 2021gno, an He-rich CaRT (Jacobson-Galán et al. 2022). We identify Ca II $\lambda\lambda$3933 and 3968, Mg II λ4481, N III λ4638, C III λ4658, C IV λ5801, He I λ5876, Si II λ6347, C II λ6580, and O I λ7775 with blue vertical lines. Note that He I λ5876 is only seen in the spectra of SN 2021gno. All spectra are in the rest frame. The vertical axis is scaled linearly. The earliest spectrum is presented in Zimmerman et al. (2022). The SN 2022oqm and SN 2021gno spectral sequences are available as the data behind the figure. This includes the "Earth"-frame (uncorrected) observations of SN 2022oqm.

(The data used to create this figure are available in the online article.)

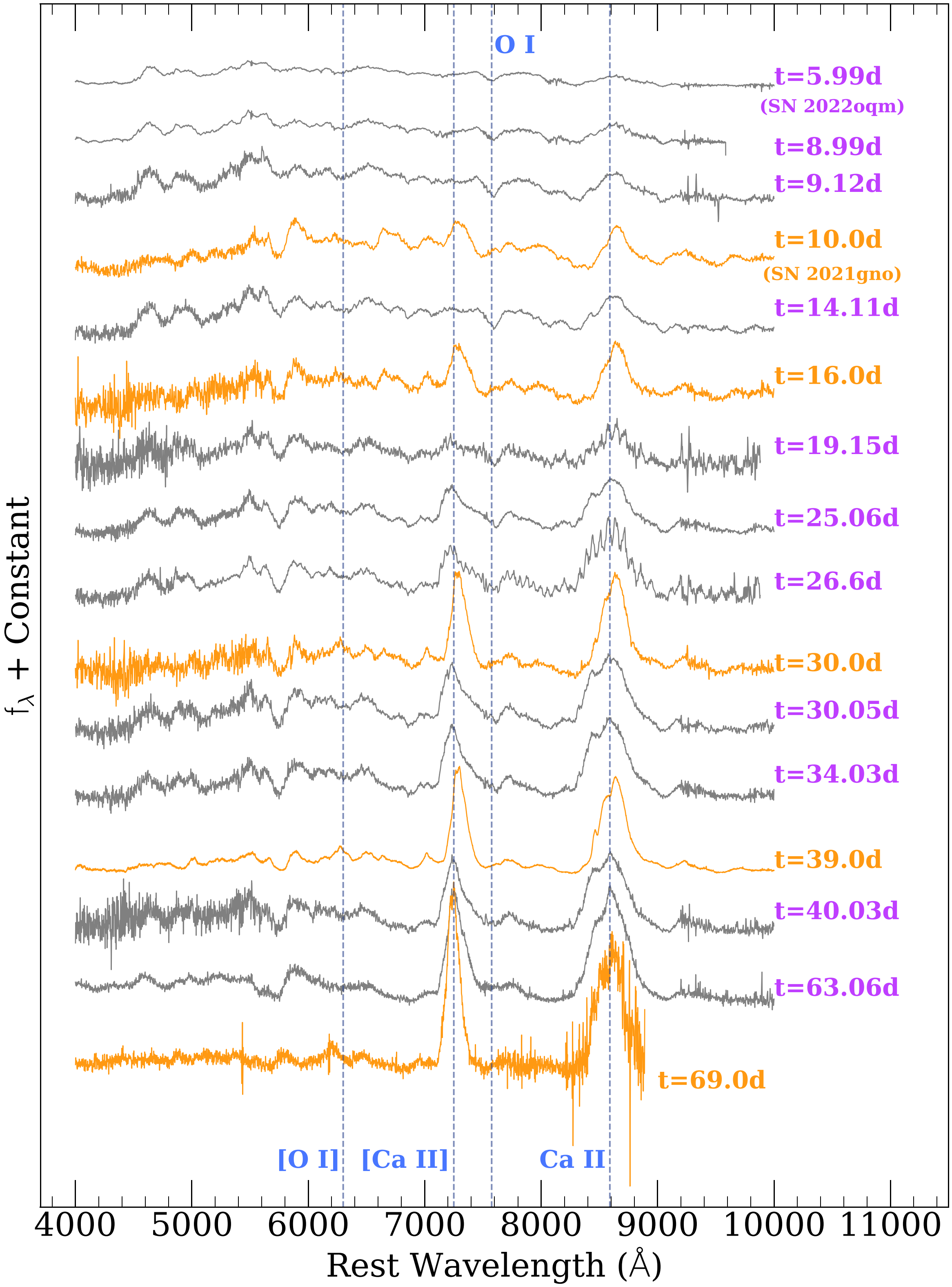

Figure 6. Spectral sequence of SN 2022oqm during 5 days $\leqslant t \leqslant$ 65 days, overlaid with the same-phase spectra of the He-rich CaRT SN 2021gno (Jacobson-Galán et al. 2022). The features O I λ7775, [Ca II] $\lambda\lambda$7291, 7324, and Ca II $\lambda\lambda$8498, 8542, and 8662 Å are clearly detected and marked. We also show the location of [O I] $\lambda\lambda$6300, 6364, but this line is not clearly detected in our spectral sequence. The strong [Ca II] $\lambda\lambda$7291, 7324 feature is characteristic of CaRTs. The Ca complex found redward of 8000 Å is a permitted feature and is not used to qualify a transient as a CaRT. All spectra are in the rest frame. The vertical axis is scaled linearly. The SN 2022oqm and SN 2021gno spectral sequences are available as the data behind the figure. This includes the "Earth"-frame (uncorrected) observations of SN 2022oqm.

(The data used to create this figure are available in the online article.)

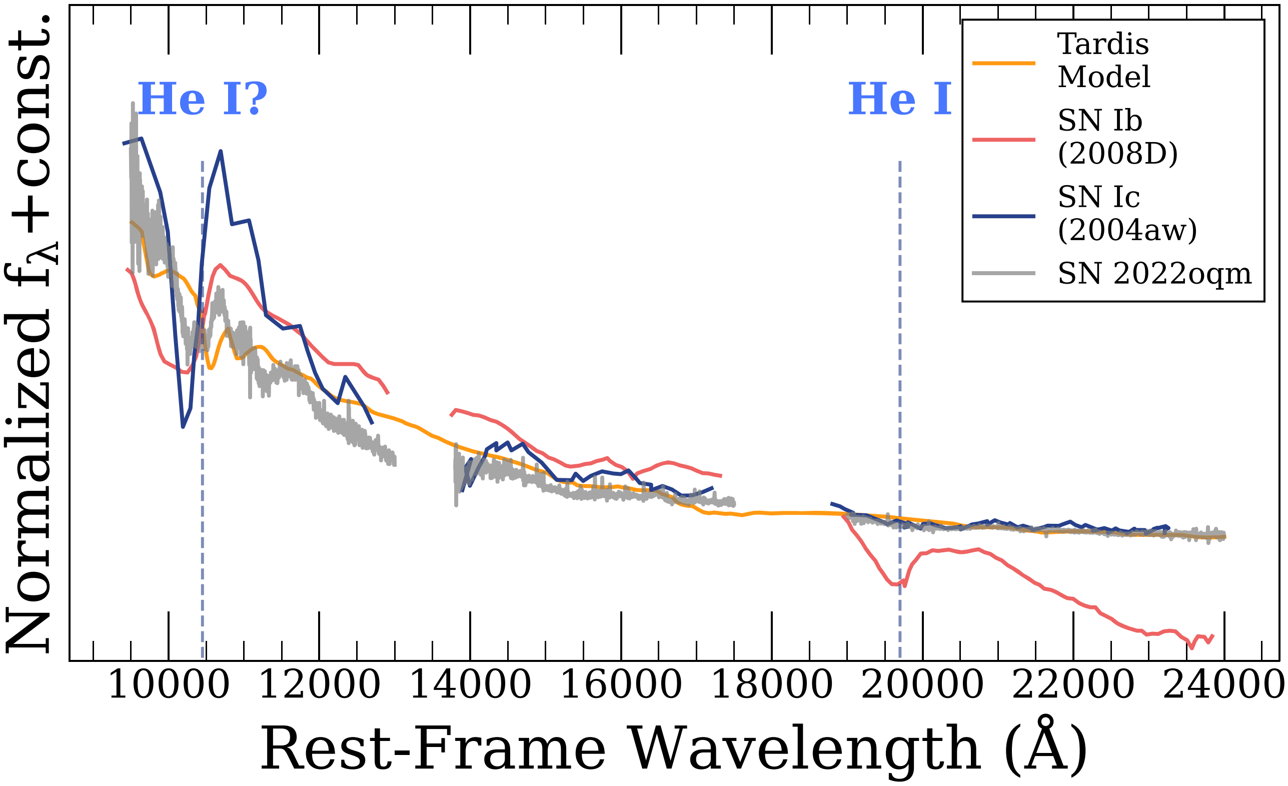

Figure 7. NIR Spectrum of SN 2022oqm taken at $t = -4.9$ days in gray. Also overlaid are the corresponding phase `TARDIS` radiative transfer simulation (see Figure 10) in orange, the NIR spectrum of the SN Ib SN 2008D in red, and the NIR spectrum of the SN Ic SN 2004aw in dark blue. In contrast to SN 2022oqm, SN 2008D has clear He I λ10830 and He I λ20581 absorption features. Similar to SN 2022oqm, SN 2004aw has a potential He I λ10830 absorption feature, but lacks the He I λ20581 absorption feature. The spectrum of SN 2004aw is from Taubenberger et al. (2006) and the spectrum of SN 2008D is from Modjaz et al. (2009). The vertical axis is scaled linearly. The NIR spectra and TARDIS model are available as the data behind the figure.

(The data used to create this figure are available in the online article.)

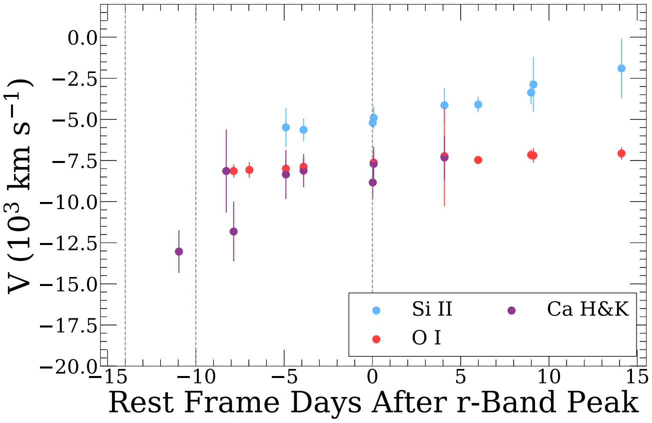

Figure 8. Velocities of the Si II, O I, and Ca H&K absorption lines measured during the photospheric phase. Silicon is consistently at a smaller velocity (and therefore radius) than oxygen and calcium, which seem to be at similar radius throughout the early evolution. Times of peaks 1, 2, and 3 are shown as dotted gray lines. The absorption line velocities are available as the data behind the figure.

(The data used to create this figure are available in the online article.)

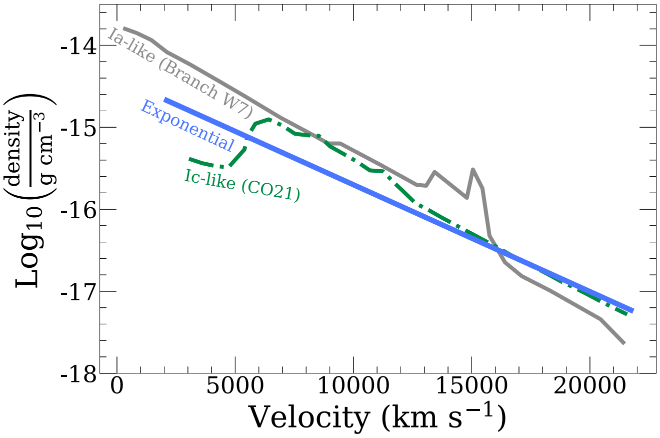

Figure 9. We use the exponential ejecta mass density profile to model SN 2022oqm ejecta using `TARDIS`. This is shown in relation to two commonly used density profiles for SN Ia and SN Ic modeling. The exponential density profile, which is shallower than both the Ia-like and Ic-like profiles, provides the best fit to the SN 2022oqm ejecta spectra. The fitted spectra are shown in Figure 10. The density profiles are available as the data behind the figure.

(The data used to create this figure are available in the online article.)

transient: $t_{\rm d} \propto \sqrt{\kappa m_{\rm ej}/v_{\rm ej}}$. As such, we present $t_{\rm d}$ in addition to these three parameters.

5.1. Joint Shock Cooling and Radioactive Decay Model

First, we explore a toy model in which the emission can be modeled by the combination of a power-law model (a reasonable description for shock cooling) and a radioactive decay model. The first peak would be captured by the power-law model and the subsequent LC evolution would be captured by the radioactive decay. For the power-law model, we utilize a power-law source of bolometric luminosity,

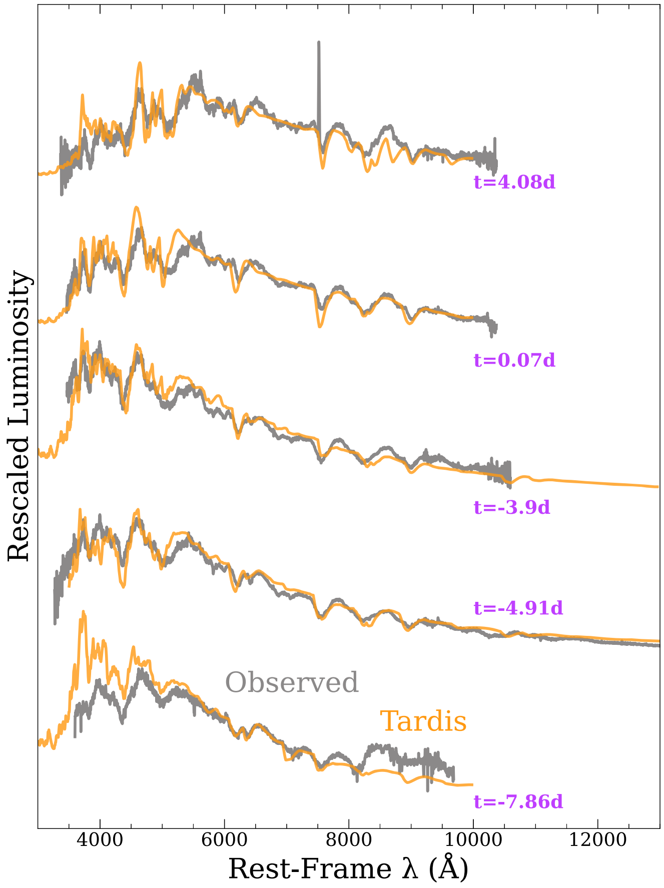

Figure 10. Spectral series of SN 2022oqm (gray curves) and the corresponding `TARDIS` radiative transfer simulation (orange curves). We find good agreement between the `TARDIS` models and our observed spectral sequence. The vertical axis is scaled linearly. The inferred ejecta density profile and the ejecta abundances, as inferred from `TARDIS` are shown in Figures 9 and 11, respectively. The SN 2022oqm and TARDIS spectral sequences are available as the data behind the figure. This material includes the TARDIS parameter files.

(The data used to create this figure are available in the online article.)

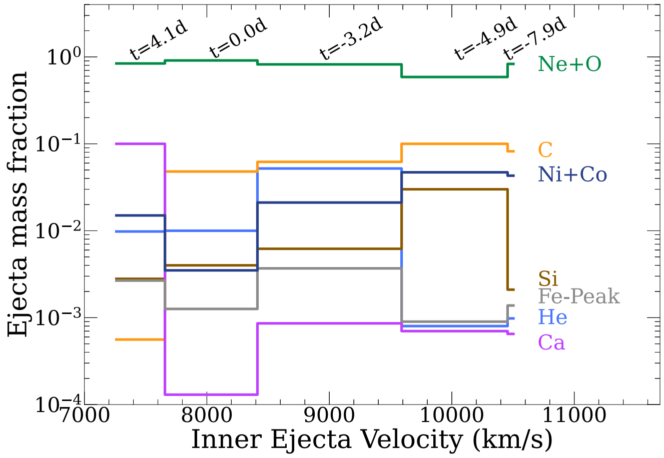

Figure 11. The abundance pattern derived from `TARDIS` fitting to spectra at $t = -7.86$, -3.22, 0.07, and 4.08 days. Atomic abundances that are degenerate via `TARDIS` modeling are combined into one category (i.e., Ne+O, Ni+Co, and Fe-Peak, which is Fe, Ti, and Cr). The distributions of Fe-peak elements, radioactive elements, and lower-mass elements are flat throughout the ejecta. The abundance patterns are available as the data behind the figure.

(The data used to create this figure are available in the online article.)

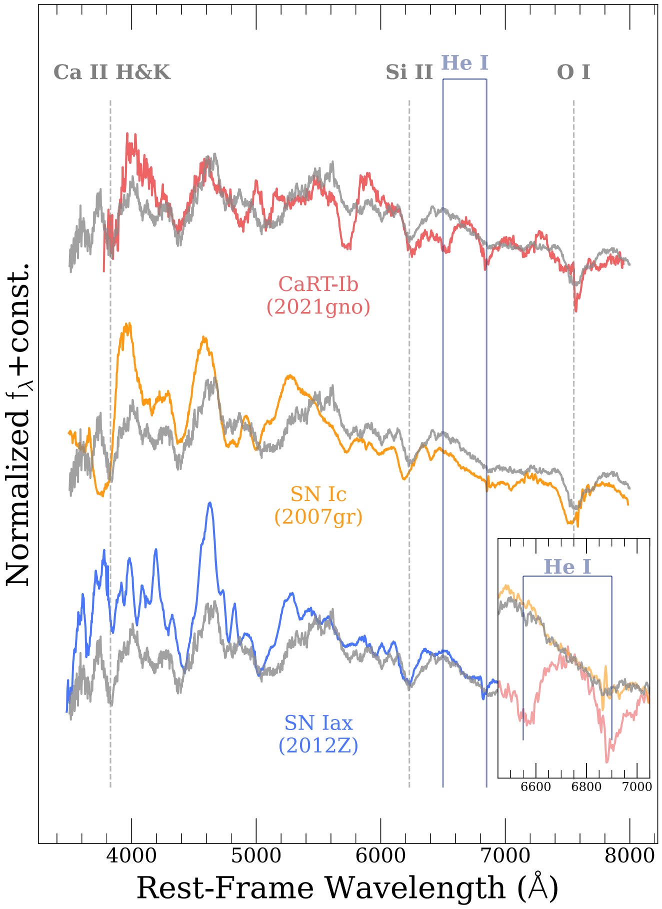

Figure 12. Peak-time spectrum of SN 2022oqm (gray) overlaid with peak-time spectra of SN 2012Z (SN Iax), SN 2007gr (SN Ic), and SN 2021gno (CaRT). Absorption lines visible in the spectrum of SN 2022oqm are marked. SN 2022oqm appears quite similar to SN Iax, SN Ic, and the CaRT. We show Ca II $\lambda 3933$ Å, Si II $\lambda 6347$, He I $\lambda 6678$, He I $\lambda 7065$, and O I $\lambda 7775$, where the helium lines are only clearly discernable in the CaRT-Ib spectrum. The peak-time spectra are available as the data behind the figure.

(The data used to create this figure are available in the online article.)

described by:

$$L_1 = L_{\rm pow}(t/t_{\rm pow})^{-\alpha}, \tag{1}$$

where $L_{\rm pow}$ is a luminosity scaling factor, $t_{\rm pow}$ is the timescale of decay, and α is the power-law index. This emission is treated as a single blackbody, with a characteristic photosphere velocity $v_{\rm ej,\ pow}$, opacity $\kappa_{\rm pow}$, and minimum photosphere temperature $T_{\rm pow}$ (see Villar et al. 2017; Guillochon et al. 2018 for more details).

We note that the power-law model is a well-known model to describe the luminosity of shock-heating material over time (see, e.g., Nakar & Sari 2010; Piro et al. 2021). In this case, the time dependence is directly linked to the outer ejecta profile, $L_1 \propto t^{-4/(n-2)}$, where n is the index of the power law that describes the outer ejecta density profile. We also note that we do not allow for photons emitted via this power-law model to diffuse through any material after emission. This is equivalent to assuming there is no material beyond the region where these power-law photons are emitted that can diffuse photons. Allowing diffusion of the power-law photons results in a much poorer fit (see Appendix B, where we attempt this fit).

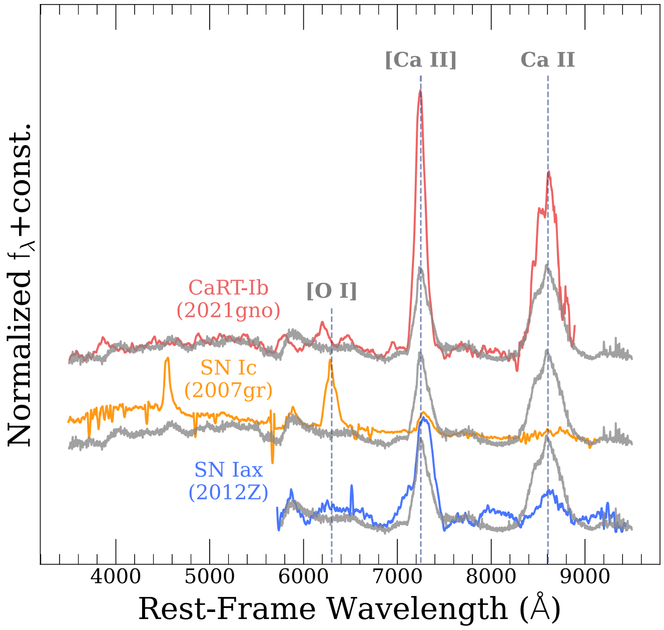

Figure 13. Nebular spectrum of SN 2022oqm (gray) overlaid with nebular spectra of SN 2012Z (SN Iax), SN 2007gr (SN Ic), and SN 2021gno (CaRT). The [Ca II] $\lambda\lambda$7291, 7324 forbidden emission line is present in all spectra but is strongest in the CaRTs. The [O I] $\lambda\lambda$6300, 6364 feature is completely absent in the spectrum of SN 2022oqm. Note that this [O I] line is stronger in the SN Ic, a characteristic difference between SNe Ic and Ca-Ic. The nebular spectra are available as the data behind the figure.

(The data used to create this figure are available in the online article.)

The radioactive decay of ^{56}Ni produces gamma rays that are thermalized in optically thick ejecta, which then emit as a blackbody, driving peaks 2 and 3 (Arnett 1982; Chatzopoulos et al. 2012; Villar et al. 2017). The free parameters corresponding to this are the ^{56}Ni mass (m_{Ni}) and diffusion time $t_{\mathrm{d}} \propto \sqrt{\kappa m_{\mathrm{ej}}/v_{\mathrm{ej}}}$ (see Power Law + Single ^{56}Ni Decay column in Table 3).

We present the fitted LC in Figure 14, and show the fitted parameters in Table 3. We overall find agreement between the model and data ($\chi^2_{\mathrm{red}} = 1.41$), but the fit is poor in the U, $UVW1$, and $UVM2$ bands. Most notably, this model overpredicts the emission in $UVM2$ by ~1 mag after peak 1.

5.2. Capturing Individual Peaks with Radioactive Decay Models

To find a better fit than was shown in Section 5.1, we focus on only peak 3. We cut peaks 1 and 2 from the LC by including only data points from $t > -6$ days and fit a single radioactive decay model. We find an ejecta mass of 0.55 $M_\odot$, with an ^{56}Ni fraction $f_{\mathrm{Ni}} \approx 0.16$, corresponding to ^{56}Ni mass $m_{\mathrm{Ni}} = 0.09\,M_\odot$. Even though the first two peaks have been removed for this fit, the best fit still requires all 0.09 $M_\odot$ to power peak 3, hinting that a single radioactive decay model of ^{56}Ni does not fully account for the photons emitted during peak 3.

We attempt to fit peaks 2 and 3 with a toy "two-zone" model, by considering two discrete ^{56}Ni central sources. This is similar to Maeda et al. (2003), who presented a similar formalism of a two-zone model by constructing two concentric sources of photons. Photons emitted by ^{56}Ni located at larger radii diffuse through a total mass $m_{2,\mathrm{ej}}$, before escaping from the system and driving peak 2. Photons emitted from the ^{56}Ni decay that are located deeper inside the ejecta would diffuse through a larger amount of mass ($m_{1,\mathrm{ej}} + m_{2,\mathrm{ej}}$) before escaping, resulting in the delayed, third peak.

We create a custom model in `MOSFiT` to perform this fit. We find an inner ejecta layer with mass of $\log_{10}\,[m_{1,\mathrm{ej}}/M_\odot] = 0.07^{0.16}_{0.21}$ and an ^{56}Ni fraction of $\log_{10} f_{1,\,\mathrm{Ni}} = -1.30^{0.21}_{0.16}$, corresponding to $\log_{10}\,[M_{1,\mathrm{Ni}}/M_\odot] = 0.055^{0.002}_{0.002}$ of ^{56}Ni. We find an outer ejecta layer with mass of $\log_{10}\,[m_{2,\mathrm{ej}}/M_\odot] = -0.96^{0.15}_{0.27}$ and an ^{56}Ni fraction of $\log_{10} f_{2,\,\mathrm{Ni}} = -0.49^{0.25}_{0.17}$, corresponding to $\log_{10}\,[M_{2,\mathrm{Ni}}/M_\odot] = 0.04^{0.002}_{0.002}$ of ^{56}Ni.

5.3. Joint Shock Cooling and Double Radioactive Decay Model

Finally, we combine the power-law model of peak 1 to the Double ^{56}Ni Decay model of peaks 2 and 3 to fit the entire LC. In such a model, peak 1 is powered by shock cooling of the CSM following shock breakout. Peak 2 is powered by radioactive decay of ^{56}Ni distributed near the outer regions of the ejecta. Peak 3 is powered by radioactive decay of ^{56}Ni distributed near the inner regions of the ejecta. Photons emitted from the inner regions of the ejecta diffuse through more mass and take longer before they are emitted. We show a schematic of this model in Figure 15. We find a power-law index of $\alpha = 4.55^{0.78}_{0.95}$, $\log_{10}\,[L_{\mathrm{pow}}/\mathrm{erg\ s^{-1}}] = 41.43^{1.79}_{1.15}$, $\log\,[t_{\mathrm{pow}}/\mathrm{days}] = 0.71^{0.30}_{0.35}$ days. The inner layer of ejecta has $\log_{10}\,[m_{1,\mathrm{ej}}/M_\odot] = -0.35^{0.07}_{0.06}$ and ^{56}Ni mass of $m_{1,\mathrm{Ni}} = 0.055^{0.002}_{0.001}\,M_\odot$. The outer layer of ejecta has $\log_{10}\,[m_{2,\mathrm{ej}}/M_\odot] = -0.73^{0.08}_{0.11}$ and ^{56}Ni mass of $m_{\mathrm{Ni},2} = 0.040^{0.002}_{0.003}\,M_\odot$. The total ejecta mass from this model is $\log[(m_1 + m_2)/M_\odot] = -0.2 \pm 0.11$, and $m_{1,\mathrm{Ni}} + m_{2,\mathrm{Ni}} \approx 0.09\,M_\odot$ of it is ^{56}Ni.

Compared to the model presented in Section 5.1, our joint Power Law + Double ^{56}Ni decay provides a better fit to the SN 2022oqm photometry. We obtain a WAIC score of 758 and reduced $\chi^2_{\mathrm{red}} \approx 1$. This suggests that the SN 2022oqm LC is powered by three distinct sources, leading to the triple peaked behavior seen in Figure 2.

We note here that all three peaks are not clearly visible in all bands. Rather, peak 1 is most clearly visible in UV bands, e.g., Swift; peaks 1 and 2 are visible in slightly longer wavelengths, e.g., u-band; and peak 3 is strongest in longer wavelengths, e.g., the r-band. To clearly visualize these peaks, we overlay the data in these bands with our `MOSFiT` models in these three regimes in the right panel of Figure 16.

5.4. Reflections on Photometric Modeling

Through Sections 5.1, 5.2, and 5.3, we find that

1. Peaks 2 and 3 can be modeled as two distinct radioactive peaks.
2. The total nickel mass is ~0.09 $M_\odot$.
3. Peak 1 can be modeled with a power-law model of emission in time, suggesting a shock cooling peak.

The presence of narrow, highly ionized emission lines in the earliest spectrum also suggests emission from shocked material during the first ~2 days of this SN (see Section 4). We capture peak 1 with a power-law index $\alpha = 4.55$. Piro et al. (2021) show that shock cooling emission following an astrophysical explosion can be captured by a power-law emission in time $t^{-4/(n-2)}$, where n is the radial dependence of density in the outer region of the ejecta upon radius. Piro et al. (2021) then

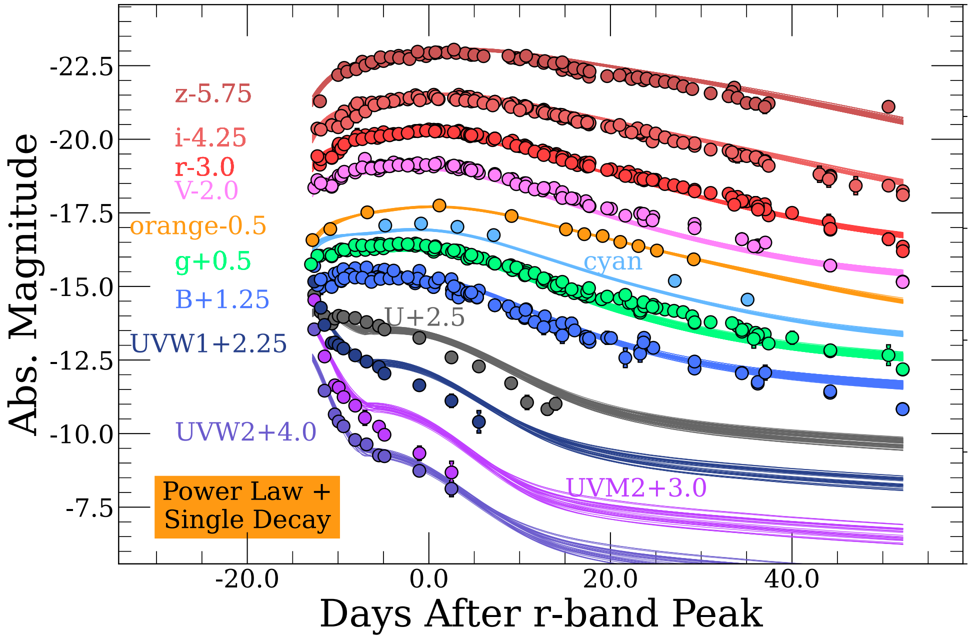

Figure 14. Best-fit model to the UVONIR LCs for the shock cooling ^{56}Ni model. Points represent observed photometry, while colored lines are random draws from the resulting posterior. Fitting is done using the `MOSFiT` package.

Table 3
Best-fit Parameters of Each Model Produced in `MOSFiT`

Module	Parameter	Power Law + Single ^{56}Ni Decay (Section 5.1)	Single ^{56}Ni Decay (Section 5.2)	Double ^{56}Ni Decay (Section 5.2)	Power Law + Double ^{56}Ni Decay (Section 5.3)
Power Law	$\log \frac{L_{\rm pow}}{\rm erg\ s^{-1}}$	$43.43^{0.89}_{1.17}$	…	…	$41.43^{1.79}_{1.15}$
	α	$1.10^{0.03}_{0.03}$	…	…	$4.55^{0.78}_{0.95}$
	$\log \frac{t_{\rm pow}}{\rm days}$	$-0.5^{1.11}_{0.83}$	…	…	$0.71^{0.3}_{0.35}$
	$\log \frac{v_{\rm ej,\ pow}}{\rm km\ s^{-1}}$	$4.14^{0.03}_{0.05}$	…	…	$3.82^{0.09}_{0.1}$
	$\kappa_{\rm pow}$	$0.11^{0.05}_{0.03}$	…	…	$0.11^{0.05}_{0.04}$
	$\log \frac{T_{\rm pow}}{\rm K}$	$3.79^{0.01}_{0.01}$	…	…	$3.43^{0.41}_{0.27}$
^{56}Ni Decay 1	$\log \frac{m_{1,\ \rm ej}}{M_\odot}$	$-0.41^{0.01}_{0.01}$	$-0.26^{0.02}_{0.02}$	$0.07^{0.16}_{0.21}$	$-0.35^{0.07}_{0.06}$
	$\log f_{1,\ \rm Ni}$	$-0.70^{0.01}_{0.01}$	$-0.79^{0.03}_{0.02}$	$-1.30^{0.21}_{0.16}$	$-0.90^{0.04}_{0.06}$
	$M_{1,\ \rm Ni}$	$0.074^{0.001}_{0.001}$	$0.09^{0.003}_{0.002}$	$0.055^{0.002}_{0.002}$	$0.06^{0.002}_{0.002}$
	$\log \frac{v_{1,\ \rm ej}}{\rm km\ s^{-1}}$	$4.0^{0.02}_{0.02}$	$4.31^{0.01}_{0.01}$	$3.97^{0.01}_{0.02}$	$3.92^{0.02}_{0.01}$
	$\log \frac{T_1}{\rm K}$	$2.7^{0.39}_{0.42}$	$3.68^{0.01}_{0.0}$	$2.82^{0.28}_{0.62}$	$2.57^{0.54}_{0.38}$
	$\log \kappa_{\gamma,12}$	$-0.98^{0.03}_{0.02}$	$-0.99^{0.02}_{0.01}$	$-0.40^{0.21}_{0.15}$	$-0.99^{0.02}_{0.01}$
	$\kappa_{1,2}$	$0.18^{0.01}_{0.01}$	$0.19^{0.0}_{0.01}$	$0.10^{0.05}_{0.04}$	$0.19^{0.00}_{0.01}$
	$\log \frac{t_{\rm d}}{\rm days}$	$1.09^{0.08}_{0.9}$	$0.78^{0.01}_{0.01}$	$1.1^{0.02}_{0.02}$	$1.1^{0.01}_{0.03}$
^{56}Ni Decay 2	$\log \frac{m_{2,\ \rm ej}}{M_\odot}$	…	…	$-0.96^{0.15}_{0.27}$	$-0.73^{0.08}_{0.11}$
	$\log f_{2,\ \rm Ni}$	…	…	$-0.49^{0.25}_{0.17}$	$-0.67^{0.11}_{0.08}$
	$M_{2,\ \rm Ni}$	…	…	$0.04^{0.002}_{0.002}$	$0.04^{0.002}_{0.003}$
	$\log \frac{v_{2,\ \rm ej}}{\rm km\ s^{-1}}$	…	…	$4.21^{0.03}_{0.03}$	$4.06^{0.03}_{0.02}$
	$\log \frac{T_2}{\rm K}$	…	…	$3.78^{0.01}_{0.01}$	$3.76^{0.01}_{0.01}$
	$\log \kappa_{\gamma,12}$	…	…	$-0.40^{0.21}_{0.15}$	$-0.99^{0.02}_{0.01}$
	$\kappa_{1,2}$	…	…	$0.10^{0.05}_{0.04}$	$0.19^{0.00}_{0.01}$
	$\log \frac{t_{\rm d}}{\rm days}$	…	…	$0.46^{0.06}_{0.06}$	$0.81^{0.04}_{0.05}$
General	$\log \sigma$	$-0.65^{0.01}_{0.02}$	$-0.43^{0.04}_{0.02}$	$-0.71^{0.01}_{0.01}$	$-0.73^{0.01}_{0.01}$
	WAIC	705.1	550.4	727.1	822.9
	$\chi^2_{\rm red}$	1.29	3.53	1.52	0.85

Note. The goodness of fit is parameterized by the Watanabe Akaike Information Criterion (WAIC) measure and by the reduced chi-squared ($\chi^2_{\rm red}$) measure.

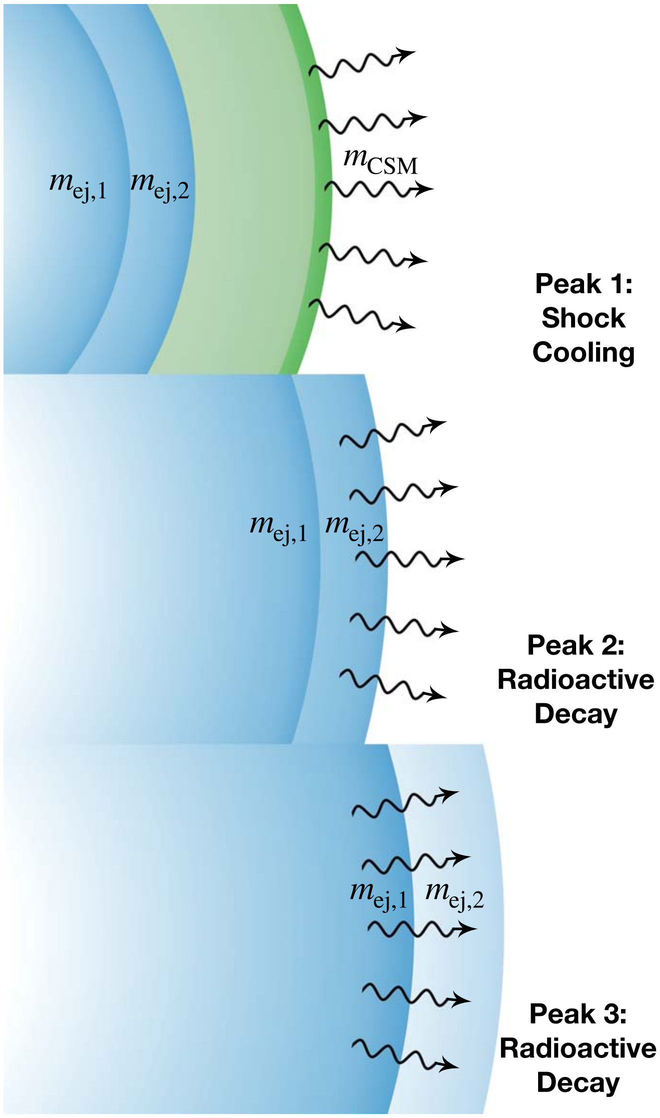

Figure 15. Schematic to highlight the sources of photons during peaks 1, 2, and 3 in our shock cooling-double-decay model (Section 5.3). Fits to this model are shown in Figure 16 and the fitted parameters are shown in the far-right column of Table 3.

connect n to s, the polytropic index of the exploding star: $n = (1 + 1/s + 3\beta)/\beta$, where $\beta \approx 0.19$. Following this, our fitted value of $\alpha = 4.55$ results in a polytropic index of $s \approx -0.9$, an unphysical value. Likely, more precise prescriptions of early emission are necessary to describe the early light-curve behavior. We attempt fitting the model of Morag et al. (2023, hereafter, M23) to peak 1, and find that this fit does not converge to the photometry of SN 2022oqm. Furthermore, this model finds total ejecta mass ($0.63\,M_\odot$) is within 1σ of the mass found by spectroscopic modeling ($\approx 0.6\,M_\odot$, see Section 4), which shows independent support to the best-fit light-curve model we use here. As such, we consider inferred physical properties from the best self-consistent model of the LC explored: the combination of a power-law shock cooling emission model and a double ^{56}Ni decay model.

We emphasize that our double ^{56}Ni decay model is a toy approximation for a multizone model. Our model suggests that the LC is powered by a centrally located radioactive material, with a fraction of Fe-peak elements mixed into the outer ejecta layers. In particular, the fact that the best-fit model requires that at least some radioactive material is not centrally located hints at the mixing of ^{56}Ni throughout the ejecta. The mixed distribution of ^{56}Ni throughout the ejecta is consistent with our spectroscopic modeling (see Figure 11). The outer ejecta layer is less massive, more nickel rich, and faster moving than the inner ejecta layer. In addition, such agreement with such a two-zone model of SN emission highlights the need for more robust multidimensional analytical models of SNe emission (Maeda et al. 2003).

It is worth noting that Irani et al. (2022) also find that fitting the first peak to the model of Piro et al. (2021) results in an unphysical fit. Irani et al. (2022) then instead fit the photometry during only peak 2 to a combined ^{56}Ni radioative decay + M23 model and find agreement to the photometry. After peak 2, they find agreement with an independent ^{56}Ni radioactive decay model. Therefore, the Irani et al. (2022) interpretation of the multiple peaks of SN 2022oqm is one of CSM interaction during peak 1, shock cooling and ^{56}Ni radioactive decay during peak 2, and only ^{56}Ni radioactive decay during peak 3.

6. Comparing to the CaRT Population

SN 2022oqm is the 39th transient to be classified as a CaRT. We present an aggregate list of all known CaRTs at the time of writing in Table 5, along with the original references and basic observational properties. Although the prototypical CaRT is SN 2005E (Perets et al. 2010), several CaRTs were detected before 2005 (see Table 5). The most comprehensive study of CaRTs observed before 2020 is presented in De et al. (2020). Since then, 11 CaRTs have been presented in detail by Jacobson-Galán et al. (2020a), Das et al. (2022), and Jacobson-Galán et al. (2022).[39]

In Figure 17, we compare the r-band peak absolute magnitude and the Philips-like measure ΔM_7 (change in r-band magnitude during the 7 days after r-band peak) of SN 2022oqm to those of the populations of CaRTs-Ibc, the Drout et al. (2011) population of SNe Ibc, and a sample of SN Ia light curves. We generate our SN Ia LC sample using an empirical relation described by Tripp & Branch (1999) and Betoule et al. (2014):

$$t_{\rm dur} = 35s \text{ days}, \tag{2}$$

$$M_{\rm peak,r} = -19.2 - 1.4(s - 1.0), \tag{3}$$

where s parameterizes the light-curve stretch, for which we provide a range of 0.6–4. We use the canonical $s = 1$ model from Nugent et al. (2002) to find a template R-band LC to stretch using s. De et al. (2020) presented ΔM_7 instead of the canonical ΔM_{15} (Phillips 1993) because CaRTs often evolve too quickly to have a complete enough LC to measure ΔM_{15}. We adopt the measure of ΔM_7 for the full population of CaRTs from the samples of De et al. (2020), Das et al. (2022), and from detailed analyses of these objects (Chu et al. 2007; Perets et al. 2010; Kasliwal et al. 2012; Prentice et al. 2020; Zheng & Yu 2021; Jacobson-Galán et al. 2022). SN 2022oqm is among the brightest of all known CaRTs. It has a peak light magnitude

---

[39] Note though SNe Iax have CaRT-like nebular spectra, and their late-time Ca emission strength would place them in the realm of CaRTs, we do not however consider them CaRTs for this analysis. See Foley et al. (2013) for a detailed analysis of the $\gtrsim$25 members of this class.

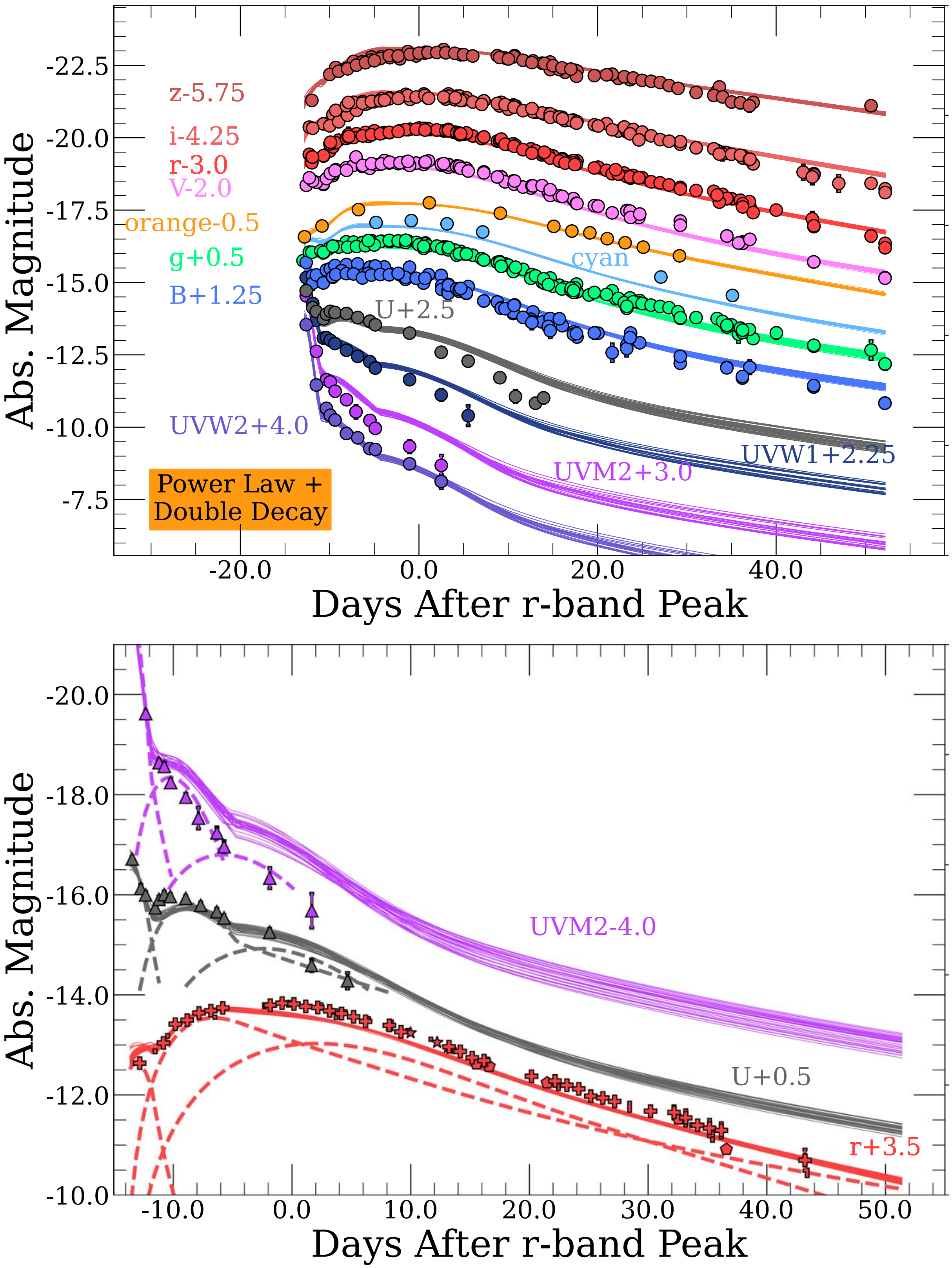

Figure 16. (Top): the result of fitting shock cooling and the double Arnett model to the photometry of peaks 1, 2, and 3. In agreement with the double Arnett model, this fit finds a total ^{56}Ni mass of $\sim 0.09\,M_{\odot}$, with total ejecta mass $\sim 1 M_{\odot}$. (Bottom): contribution to *r*-, *U*-, and *UVM*2-band light curves from the three sources of photons. Peak 1 is powered by shock interactions with CSM, and is most clearly visible in UV bands. Peak 2 is powered by the radioactive decay of ^{56}Ni in the outer ejecta, and is most clearly visible in the *U*-band. Because photons emitted by this overdensity of ^{56}Ni have less mass to diffuse through, they will be observed before photons emitted by ^{56}Ni in more inner regions of the ejecta. Peak 3, which is most clear in the *r*-band, is powered by the radioactive decay of ^{56}Ni in the inner ejecta. Fitting is done using the `MOSFiT` package.

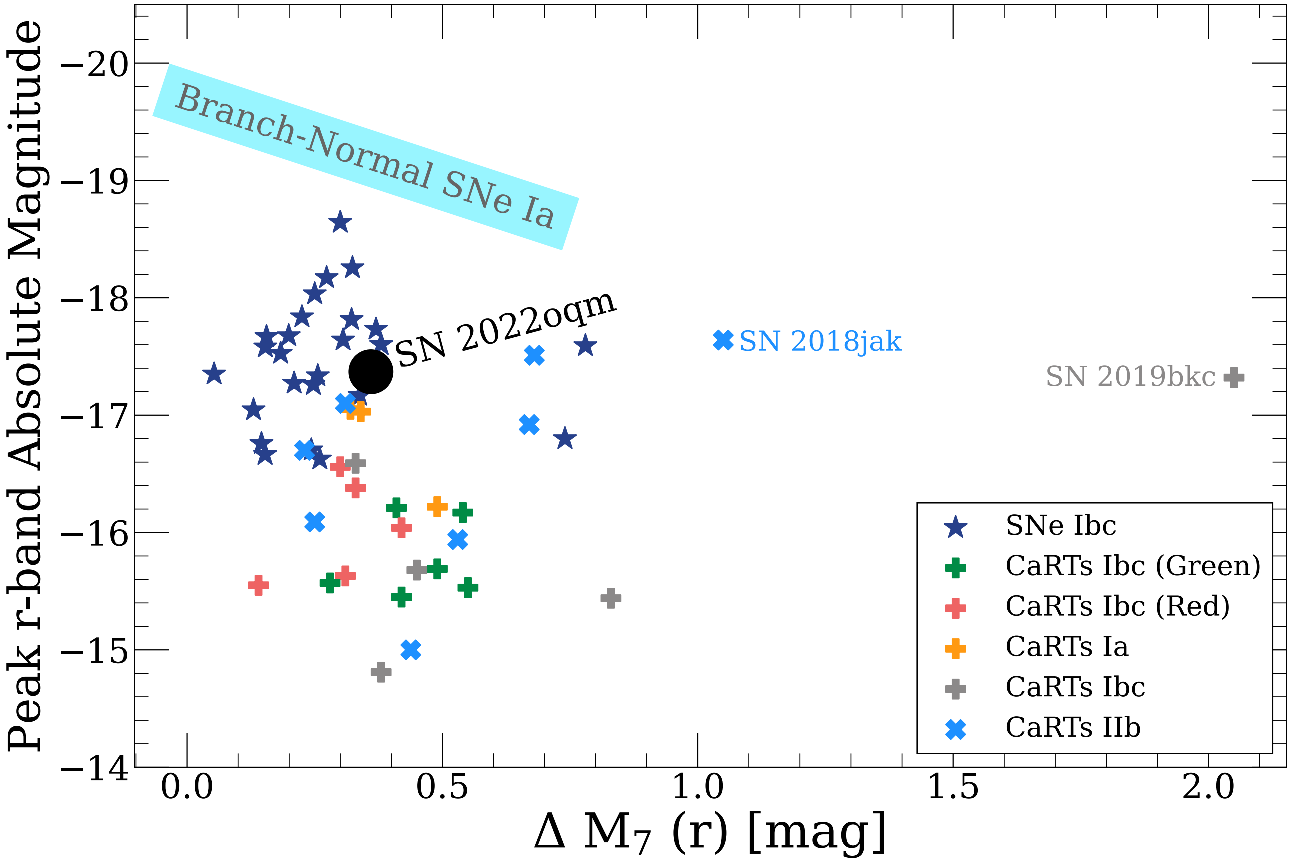

Figure 17. Comparison of the decline rate and absolute magnitude for CaRTs, SNe Ibc, and SNe Ia. These SNe Ibc are presented in Drout et al. (2011). We generate the sample of Branch-Normal SNe Ia using the methodology described in Equations (2) and (3). CaRTs Ia, Green CaRTs Ibc, and Red CaRTs Ibc are presented in De et al. (2020). SN 2022oqm is among the brightest CaRTs detected. Its peak *r*-band absolute magnitude is typical of SNe Ibc. CaRTs Ibc shown as gray pluses are unclassified as Green or Red either because the De et al. (2020) sample predates their discovery or because De et al. (2020) did not classify them as Green or Red. These are SN 2007ke (Chu et al. 2007; Perets et al. 2010), PTF11bij (Kasliwal et al. 2012), SN 2019bkc (Chen et al. 2020; Prentice et al. 2020; Zheng & Yu 2021), SN 2021gno (Jacobson-Galán et al. 2022; Ertini et al. 2023), and SN 2021inl (Jacobson-Galán et al. 2022). The sample of CaRTs IIb is presented in Das et al. (2022). The underlying measurements are available as the data behind the figure.

(The data used to create this figure are available in the online article.)

Table 4
Comparison of SN 2022oqm to Parameters of Red and Green CaRTs-Ibc from De et al. (2020)

Observable	Ca-Ibc Red	Ca-Ibc Green	SN 2022oqm
Si II?	strong to weak	weak	weak
He I?	weak to strong	strong	weak
$V(10^3\ \mathrm{km\ s^{-1}})$	4–10	8–12	∼8
Blanketed?	yes	no	yes
M_{peak}	−15.3–16.7	−15.5–16.2	∼ −17
Δm_7	0.3	0.5	0.3
$g - r$	1.5	0.4	0.5
[Ca II]/[O I]	2.5–10	7–13	4.3

Notes. These comparisons suggest SN 2022oqm is a red Ca-Ibc, with the exceptions that the $g - r$ color of SN 2022oqm suggests that SN 2022oqm is more like a green Ca-Ibc and that the peak magnitude for SN 2022oqm is much brighter than that of both classes. We find that SN 2022oqm is very likely a Ca-Ibc, and propose that SN 2022oqm may be a transition object between red and green CaRTs-Ibc.

that is characteristic of most SNe Ibc, but evolves faster than most SNe Ibc.

De et al. (2020) classify the population of CaRTs observed before 2020 into Ia-like CaRTs (CaRTs-Ia) and Ibc-like CaRTs (CaRTs-Ibc). SN 2022oqm shows many similarities with the CaRTs-Ibc class (see Table 4). They further classify CaRTs-Ibc into “Red” CaRTs-Ibc and “Green” CaRTs-Ibc. Red CaRTs-Ibc have somewhat redder spectra, due to line blanketing of flux in shorter wavelengths, lower ejecta velocity, somewhat brighter peak magnitude, and smaller [Ca II]/[O I] ratio. Green CaRTs-Ibc have flatter spectra, with no blanketing and equal flux in longer and shorter wavelengths, higher ejecta velocities, somewhat dimmer peak magnitudes, and larger [Ca II]/[O I] emission ratio.

Each population is characterized by properties listed in Table 4, where we compare SN 2022oqm to the Red and Green CaRTs-Ibc, the only two CaRT populations with which SN 2022oqm has similarities. SN 2022oqm has many characteristics consistent with the Red Ca-Ibc population: weak signatures of Si II and He I; suppressed blue flux; has an *r*-band Philips-like measure $\Delta M_7 \approx 0.3$, and [Ca II]/[O I]≈4.3. In contrast, SN 2022oqm has a high photospheric velocity (∼8000 km s^{-1}) and bluer $g - r$ color of ∼0.5 mag, both of which are characteristic of the Green CaRTs-Ibc population. Furthermore, the peak r-band magnitude near −17 mag is unlike both populations. As such, we suggest that SN 2022oqm may be an intermediate object between the Green and Red CaRTs-Ibc populations, with multiple characteristics of each, and a peak absolute magnitude that is uncharacteristic of either classes. This may also indicate that there is a continuum between Red and Green CaRTs-Ibc, with the two subpopulations resulting from a relatively small sample size of CaRTs-Ibc.

SN 2022oqm is not the only event to fall outside of the classification scheme presented by De et al. (2020). The sample of CaRTs presented in Das et al. (2022) includes several IIb-like CaRTs, which are brighter than most CaRTs and are shown in light blue in Figure 17. Though they have brighter peak magnitudes, they appear to have a similar LC decay timescale to most CaRTs. CaRTs-IIb are likely not directly comparable to the rest of the population of CaRTs as they likely have a different progenitor system (Das et al. 2022), given their relatively bright peak magnitudes. Indeed, Das et al. (2022) suggest the progenitor of these CaRTs-IIb is a strongly stripped-envelope star with ZAMS mass of 8–12 $M_\odot$.

In addition to these, Chen et al. (2020), and Prentice et al. (2020) present the "extraordinary" supernova SN 2019bkc, a fast and bright CaRT-Ic. Similar to SN 2022oqm, SN 2019bkc has an Ic-like peak magnitude and Ic-like photospheric spectrum. As such, SN 2019bkc would have been classified as a peculiar SN Ic without a nebular spectrum, just as SN 2022oqm would have (Prentice et al. 2020). SN 2019bkc reaches a similar peak magnitude (-17.32 ± 0.04, Prentice et al. 2020) as SN 2022oqm (-17.37 ± 0.051) but decays more than 2 mag in 7 days, faster than any other known CaRT. This object is an outlier within the overall class of CaRTs-Ibc.

7. Progenitor Models for SN 2022oqm

7.1. Massive-star Progenitors

Given the early classification as an SN Ic (D. Perley et al. 2022; Fulton et al. 2022; Leadbeater 2022; Sollerman et al. 2022; see Section 2), we consider: Does SN 2022oqm have a massive-star progenitor? During the photospheric phase, the spectra of SN 2022oqm are similar to those of normal SNe Ic, displaying Ca II, Si II, and O I absorption features (see Figure 12). SN 2022oqm also peaks at $M_r = -17.37$ mag, which is typical of SNe Ic (see Figure 17).

Furthermore, the inferred ejecta mass for SN 2022oqm of 0.6 $M_\odot$ is only 1.2σ less than the mean ejecta for SNe Ic and 1.5σ and 2.5σ less than the mean ejecta mass for SNe Ib and broad-lined SNe Ic, respectively (Drout et al. 2011). The 84th percentile fitted ejecta mass (1σ greater than the mean) is $10^{-0.2+0.12}\,M_\odot = 0.81\,M_\odot$; this is $\sim$1σ less than the mean ejecta mass for SNe Ic, and 1.5σ–2σ less than the mean ejecta mass for SNe Ib and broad-lined SNe Ic (Drout et al. 2011). The ejecta mass is therefore also consistent with that of the SN Ic population.

Given the short lifetimes of high-mass progenitor stars, SNe Ic are typically found in their host galaxy's disk, often near star-forming regions (e.g., Blanchard et al. 2016). SN 2022oqm is found offset by 13.1 kpc from the center of its host galaxy. This offset, while notable, is consistent with the population of SESNe. Comparing to the Schulze et al. (2021) sample of 151 SN Ibc host-SN separations, the offset of SN 2022oqm is at the 97th percentile of all SNe Ibc. SN 2022oqm is located 2.4 half-light radii from the host center, which is greater than all but two SNe Ibc (121 events) in the Kelly & Kirshner (2012) sample: SN 2002ap (2.7 half-light radii) and SN 2007bg (3.6 half-light radii), both broad-lined SNe Ic.

An important observable of SN 2022oqm is the inferred C-, N-, and O-enhanced CSM that surrounds the exploding SN. If SN 2022oqm were a CCSN, the stripping mechanism would have needed to strip not only the hydrogen and helium layers of the progenitor star, but also sufficient carbon, nitrogen, and oxygen to excite clear signatures of them in the earliest spectrum.

A population of SESNe with markedly high stripping and low ejecta masses are ultra-stripped supernovae (USSNe). These are SESNe that have been stripped dramatically by a compact binary companion, resulting in very small ejecta masses (e.g., De et al. 2018b; Yao et al. 2020). However, USSNe are expected to have smaller ejecta masses ($m_{\rm ej} \leqslant 0.2 M_\odot$; Tauris et al. 2015), although it is possible to have higher ejecta masses in USSNe (see e.g., Sawada et al. 2022), the mass of ^{56}Ni produced by these explosions ($<$0.05 $M_\odot$) is still smaller than what is seen in SN 2022oqm. Furthermore, these progenitor systems are not expected to travel $\gtrsim$800 pc during their lifetime (Tauris et al. 2015), considerably shorter than the $\sim$3 kpc offset of SN 2022oqm from its nearest visible star-forming region. In short, a USSN origin is possible for SN 2022oqm, but not strongly favored by our observations.

There exists a small subclass of SNe Ic with ionized narrow C emission lines: SNe Icn (Gal-Yam et al. 2021). Only five SNe Icn have been identified in literature: SN 2019jc, SN 2019hgp, SN 2021ckj, SN 2021csp, and SN 2022ann (Pastorello et al. 2021; Gal-Yam et al. 2022; Pellegrino et al. 2022; D. A. Perley et al. 2022b; Davis et al. 2023). Pellegrino et al. (2022) present a fit to the light curves of four SNe Icn, combining interaction- and ^{56}Ni-powered components into a single model. For all SNe, they find that circumstellar interaction dominates the observed luminosity throughout the evolution of each SN and place upper limits of $\sim$0.04$M_\odot$ of ^{56}Ni for each SN. Davis et al. (2023) extensively studied SN 2022ann, placing an upper limit of $\sim$0.04$M_\odot$ of ^{56}Ni, and finding its emission is dominated by circumstellar interaction. Indeed all SNe Icn have narrow and ionized features at all observed phases, suggesting interactions with CSM throughout their observed spectroscopic evolution.

Of the five known SNe Icn, SN 2019jc is the most similar to SN 2022oqm. It has a relatively large host-galaxy separation (11.2 kpc, compared to 13.1 kpc for SN 2022oqm), similar g-band absolute peak magnitude (-17.2 Mag, compared to -17.3 Mag for SN 2022oqm), and similar derived ejecta mass ($\sim$0.6 $M_\odot$ for both SN 2019jc and SN 2022oqm). Moreover, SN 2019jc is also the SN Icn with the largest fitted contribution to the LC from ^{56}Ni radioactive decay. However, Pellegrino et al. (2022) infer an upper limit of 0.04 $M_\odot$ for the ^{56}Ni mass of SN 2019jc, lower than the $\sim$0.1 $M_\odot$ we infer for SN 2022oqm. It is possible that SN 2022oqm could be an SN 2019jc-like SN Icn with much less CSM and significantly more ^{56}Ni than SN 2019jc.

As such, we find that if SN 2022oqm were the result of a massive stellar explosion, it could have been an SN Icn-like event, but one that has shorter-lived (only the first $\sim$2 days post explosion) CSM interaction and a relatively large ^{56}Ni mass compared to the population. Owing to the very small observed population, the progenitor system of these SNe is not well constrained, and we are unable to consider whether a system similar to the progenitor of SNe Icn could result in an SN 2022oqm-like event.

7.2. Systems Involving an Neutron Star

A potential progenitor for SN 2022oqm is the merger of a WD-Neutron Star (NS) binary. In such a merger, the WD is tidally disrupted and sheared into an accretion disk (Metzger et al. 2008; Zenati et al. 2019a; Kaltenborn et al. 2022). Unlike the CSM commonly found around massive stars, the WD CSM is rich in helium, carbon, and oxygen. Therefore, this model could provide the necessary CO enrichment of CSM to support the detection of these lines in the spectrum during peak 1 for SN 2022oqm. Moreover, the expected magnitudes of the most massive ONe WD-NS models in principle approach those of the known CaRTs. However, these models *likely* are not bright enough to produce a 2022oqm-like SN due to low masses of radioactive material produced (Fernández et al. 2019; Zenati et al. 2020; Bobrick et al. 2022).

Another possible progenitor is one in which a short-lived magnetar with a strong surface dipole magnetic field $B_{\rm NS} \sim 10^{13} - 10^{15} G$ is born. Given that the spin down of a magnetar has been proposed as a possible source of energy in some SNe (Ostriker & Gunn 1971; Kasen & Bildsten 2010; Woosley 2010), we explore this possibility in the case of SN 2022oqm. Specifically, could the combination of spin down of a newly born magnetar and radioactive decay of the ^{56}Ni produced in the SN power SN 2022oqm? To model such a scenario, we use `MOSFiT` to combine the magnetar spin-down model and ^{56}Ni decay to model peaks 2 and 3. We find this model is an extremely poor fit to the data and does not converge to the photometry of SN 2022oqm. It cannot reduce the scatter of the fit to less than ∼5 mag of the observed photometry. Models involving the spin down of a magnetar are ordinarily invoked to obtain peak magnitudes near −20 and −21 mag, where ^{56}Ni decay cannot reasonably explain the LC of such events, e.g., in the case of Type I superluminous SNe (Nicholl et al. 2017). As such, attempting to explain the relatively low luminosity of SN 2022oqm requires a relatively weak magnetar and a small ejecta mass that are, in general, inconsistent with masses derived from spectroscopic modeling (see Section 4) and photometric modeling (see Section 5). Moreover, a magnetar is the remnant of a CCSN, which we disfavor earlier in this section. Therefore, we rule out this scenario as the progenitor system of SN 2022oqm.

Another scenario involving an NS is accretion-induced collapse: the direct collapse of a Chandrasekhar WD into a NS caused by electron capture or other processes (see Miyaji et al. 1980; Dessart et al. 2007; Metzger et al. 2009; Piro & Kulkarni 2013; Schwab 2021). Generally, such a collapse is unlikely to produce an SN, but Metzger et al. (2009) consider the possibility that such an NS could be supported by centrifugal forces owing to the fast expected spin rate, and interactions with the debris disk might create an SN-like event. In their model, Metzger et al. (2009) find that when the WD collapses into a proto-NS, if an accretion disk is formed around the NS, the disk's evolution would naturally eject $\sim 10^{-2} M_\odot$ of ^{56}Ni, and total mass $\sim 2 \times 10^{-2} M_\odot$. Photometric and spectroscopic modeling of SN 2022oqm both find larger ejecta mass and ^{56}Ni mass, with a lower ^{56}Ni fraction. Therefore, we rule out this system as the progenitor of SN 2022oqm.

7.3. WD Binaries

Several models of CaRT progenitors invoke the detonation of a helium shell on a WD (Perets et al. 2010; Fernández & Metzger 2013; Zenati et al. 2019a, 2019b, 2023; De et al. 2020). Perets et al. (2010) presented the first such explanation proposed for SN 2005E: the detonation of a $0.3\,M_\odot$ He envelope. Such a detonation would result in the overproduction of radioactive materials (Shen et al. 2010; Woosley & Kasen 2011). However, if such a detonation happens in the lower densities expected in a merging WD binary (Dessart & Hillier 2015), an overproduction of ^{56}Ni can be avoided. In addition, the He shell detonation should not trigger a core detonation, as that would result in an SN Ia (Nomoto 1982; Fink et al. 2007, 2010; Shen et al. 2019). According to Shen et al. (2019), the core detonation can be avoided if the WD mass is $\leqslant 0.8\,{\rm M}_\odot$, or if it has an O/Ne composition. De et al. (2020) suggest that CaRTs can be produced by the detonation of a helium shell on a WD, where the helium shell mass, the WD mass, and WD composition can influence whether the resulting CaRT is Ia-like or Ibc-like.

Recently Zenati et al. (2023) showed that the disruption of a low-mass C/O WD by a binary companion hybrid He+C/O WD during merger could explain the origin and properties of thermonuclear SNe with strong [Ca II] emission in their nebular spectra, including SNe Ia, peculiar SNe Ia, and CaRTs (Perets et al. 2019; Pakmor et al. 2021; Jacobson-Galán et al. 2022; Burmester et al. 2023). The accretion of C/O material onto an He+C/O WD heats its He shell, leading to a weak detonation and ejection of the shell. Liberated C/O from the disrupted WD also is sent into the surroundings. This detonation results in a Ca-rich SN while leaving the C/O core of the He+C/O WD intact as a hot remnant WD. This model predicts many of the observational features (e.g., strong nebular Ca, $B - V$ color evolution, C- and O-enhanced CSM) of SN 2022oqm, but also fails to predict others (e.g., peak luminosity, ^{56}Ni mass, ejecta mass, ejecta composition, and $r - i$ color evolution).

However, it is difficult to reproduce our inferred ejecta mass in this progenitor model. The range of fitted ejecta masses ($0.48\,M_\odot < m_{1,\rm ej} + m_{2,\rm ej} < 0.81\,M_\odot$) from photometric modeling (see Section 5) and the spectroscopically fitted ejecta mass of $\sim 0.6\,M_\odot$ (see Section 4) would imply an unexpectedly massive He+C/O WD. In particular, WDs with mass larger than $\sim 1\,M_\odot$ are associated with an O/Ne composition (Wu et al. 2022). Our spectroscopic modeling suggests that the ejecta mass fraction of C is only ∼10% and that the ejecta mass fraction of Ne could be up to ∼50% (although O/Ne are not distinguished; see Figure 11). The inferred mass and abundances may suggest instead an O/Ne WD progenitor. A more massive WD could also explain the relatively bright LC of SN 2022oqm, which is ∼1.5–2 mag more luminous than most CaRTs. However, Zenati et al. (2019b) find that in general, more massive WDs have progressively smaller helium mass fractions. Whether WDs that are massive enough to potentially explain SN 2022oqm-like explosions can have enough helium to detonate as a CaRT is still unclear. More three-dimensional, high-resolution simulations exploring the higher WD mass region parameter space are required to help further understand whether WD systems can lead to SN 2022oqm-like events.

8. Discussion

The collective observational picture of SN 2022oqm presented here showcases a highly unusual SN. SN 2022oqm was detected offset from the center of its host galaxy, NGC 5875, by 50.″6 (13.1 kpc). At the time of detection (MJD = 59771), SN 2022oqm presented a strong UV excess (peak 1). This UV excess (see Figure 2), the contemporaneous hot continuum with narrow emission lines from highly ionized atomic species (see Figure 5), the fit to the LC with a shock cooling model (see Figure 16 and Section 5), all point to CSM interaction at early times (e.g., see Tinyanont et al. 2021).

After peak 1, the LC shows a weak local maximum near MJD 59774, followed by a broader peak 3 ($\sim$ MJD 59785). The fact that the spectral sequence does not abruptly change during peaks 2 and 3 suggests that peaks 2 and 3 are caused by the same emission mechanism, rather than a result of interactions with more CSM. We find that the best fit to the photometry is given by a model that has three power sources corresponding to three photometric peaks. In this model, peak 1 is driven by shock cooling, and peaks 2 and 3 are driven by the radioactive decay of radially separated ^{56}Ni throughout the SN ejecta. Throughout its photospheric phase, SN 2022oqm appears both spectroscopically (see Figure 12) and photometrically (see Figure 17) as an SN Ic. As the SN approaches its nebular phase, a strong [Ca II]$\lambda\lambda$7291, 7324 emission feature emerges, only then revealing the "calcium-rich" nature of SN 2022oqm. At a peak *r*-band magnitude of -17.37, it is among the brightest CaRTs detected, complicating the progenitor nature of SN 2022oqm.

In Section 7, we explore possible progenitors for SN 2022oqm. Here we suggest that BWD systems with primary WD mass $M \gtrapprox 0.6 M_{\odot}$ could possibly produce (1) the C/O-enriched CSM surrounding the binary WD required to drive peak 1 and (2) the relatively bright LC within the class of CaRTs. However, such a progenitor system has difficulties. In particular, the mass we infer here is likely too large to form the He+C/O Hybrid WD required by the models of Zenati et al. (2023). The ejecta abundances we find in Figure 11 would also be inconsistent with the composition of an He+C/O WD. We find a C mass fraction of 10%, which is less than is required for He+C/O WD at these masses (Zenati et al. 2019b).

Instead, the detonation of an He shell on an O/Ne WD has been suggested as a potential CaRTs progenitor (Shen et al. 2019). Indeed, the inferred progenitor WD mass of $M \gtrapprox 0.6 M_{\odot}$ (as implied from the fitted ejecta mass) could be consistent with a WD with an O/Ne composition, the canonical composition for WDs with mass $M \geqslant 1 M_{\odot}$ (Wu et al. 2022). However, our modeling of abundances (Figure 11), which cannot distinguish between O and Ne, does not strongly constrain this possibility.

In all, the SN 2022oqm's inconsistencies with the typical model of CaRTs (e.g., peak magnitude) and with the proposed progenitor systems of CaRTs (e.g., ejecta mass and abundances) strongly point to a gap in the theoretical understanding of CaRTs. Whether a CaRTcan result from a WD with mass $\gtrapprox 0.6 M_{\odot}$ is an open question that requires dedicated theoretical study.

We also find that that SN 2022oqm could result from a massive stellar progenitor. We find that such a model would be most consistent with SNe Icn given the signs of interaction with an H- and He-free CSM and low ejecta mass. Unlike SNe Icn, SN 2022oqm does *not* show spectroscopic signatures of CSM interaction throughout the LC and has a higher inferred ^{56}Ni mass than others in the SN Icn class. Because only five SNe Icn are known (Pellegrino et al. 2022; Davis et al. 2023), the progenitor of SNe Icn is poorly constrained. Of the five known SNe Icn, four are thought to be the result of a Wolf–Rayet progenitor explosion and one (SN 2019jc, the SN Icn most similar to SN 2022oqm) the result of an USSN. Given the relatively poor constraints on the progenitor system of SNe Icn and the inconsistency in the inferred LC power source, it is unclear whether the progenitor system of SNe Icn can also give rise to an SN 2022oqm-like transient.

As such, of the progenitor systems we explore in this article, we find that SN 2022oqm might have been the result of either (1) the detonation of an He shell on a WD with mass $M \gtrapprox 0.6 M_{\odot}$ or (2) the core collapse of a highly stripped, massive star resulting in an SN Icn-like event, but with less CSM and more ^{56}Ni than all SNe Icn observed today. We emphasize that neither proposed progenitor case explains *all* observed properties of SN 2022oqm, and both progenitors are still poorly understood. However, these are the only two cases we find are able to reasonably explain many of the observed properties of SN 2022oqm.

Finally, given the photometric and spectroscopic similarity between SN 2022oqm and the SNe Ic population, we address the concern that some SN 2022oqm-like CaRTs are misclassified as SNe Ic. The relatively high peak brightness of SN 2022oqm suggests that the population of CaRTs-Ibc may have a broader range of peak magnitudes than is currently known and that, due to the absence of later-time spectroscopic follow-up observations (where a CaRT-like spectrum would have been detected), some CaRTs-Ibc have been incorrectly classified as SNe Ibc. To quantify the probability of such misclassifications, we calculate the relative rates of CaRTs-Ibc and SNe Ibc: the observed rate of SNe Ibc is $\approx$35% that of SNe Ia (the ZTF magnitude $m < 18.5$ limited survey, Perley et al. 2020), and the observed rate of CaRTs is $\approx$5% the SNe Ia observed rate (Perets et al. 2010). Therefore, the observed rate of CaRTs is $\approx 5/35 \approx 14\%$ the observed rate of SNe Ibc. Of the 28 observed CaRTs with spectroscopic subtype labels, we find that 15 are CaRTs-Ibc. Therefore, if $15/28 \approx 53\%$ of CaRTs are CaRTs-Ibc, only $\approx 53\% \times 14\% \approx 7.7\%$ of observed SNe Ibc might actually be CaRTs-Ibc. Therefore, the sample of SNe Ibc is likely not strongly contaminated by CaRTS-Ibc. However, the population of CaRTs-Ibc is possibly undercounted because many have been classified as other classes of SNe. In addition, as the Rubin Observatory is planned to begin observing in the coming months, many more transients like SN 2022oqm will inevitably be discovered. However, the upcoming Vera C. Rubin Observatory's planned cadence of $\sim$3 days presents an interesting observational challenge for the two successive radioactive decay-like peaks in SN 2022oqm. Without deliberate photometric follow-up to interweave between the planned cadence of the Rubin Observatory, such short-timescale light curves could be missed. Photometric characteristics that distinguish CaRTs from normal Type Ibc SNe in surveys such as YSE or the Rubin Observatory to enable spectroscopic follow-up are yet unexplored.

9. Conclusions

In this article, we have presented the photometric and spectroscopic observations of the recent Ic-like CaRT SN 2022oqm.

SN 2022oqm is a multipeaked CaRT with observational similarities to multiple disparate classes of SNe. It is among the brightest CaRTs known. We find that a model that combines shock cooling with the radioactive decay of two separate sources of ^{56}Ni describes the three peaks well (see Section 5.3). The first peak is well captured by a power-law model, which we ascribe to shock cooling of the CSM; and the second two peaks are captured by a "double radioactive decay" model, a rudimentary model of ^{56}Ni mixing throughout the ejecta. We find that a mass of 0.06 $M_\odot$ of ^{56}Ni in the inner portion of the ejecta, along with a mass of 0.04 $M_\odot$ of ^{56}Ni in the outer portion of the ejecta may reproduce peaks 2 and 3. The potential for ^{56}Ni mixing is further supported by detailed spectroscopic modeling of the ejecta, which predicts a flat ejecta abundance profile of iron-peak elements (see Figure 11).

We summarize our key conclusions here:

1. SN 2022oqm is an Ic-like CaRT (CaRT-Ic), with [Ca II] $\lambda\lambda$7291, 7324/[O I] $\lambda\lambda$6300, 6364 $\approx$ 4.4. Photometric evolution suggests it is most similar to the population of SNe Ibc (see Figures 3 and 17)
2. We find spectroscopic similarities with SNe Iax, SNe Ic, and other CaRTs at early photospheric phases, and similarities only with SNe Iax and CaRTs at later times. Detailed spectroscopic modeling fits SN 2022oqm with an exponential ejecta density profile, rather than the standard Ia-like (Branch W7) or the Ic-like (CO21) density profile; with a flat ejecta abundance profile for both low-mass elements and for Fe-peak elements.
3. We identify three peaks in the light curves of SN 2022oqm. Two are clearly visible in the observed light curves while the third peak emerges from modeling of the LC. The peaks are (1) an early ($\approx$0 day post explosion), blue ($B - V \approx -0.6$ mag) peak, (2) a weaker, less blue ($B - V \approx 0$ mag) peak $\approx$4 days post explosion, and (3) a third, broader peak ($B - V \approx 0.2$ mag) about $\approx$14 days post explosion. Using a combination of a power-law and two radioactive decay models, we successfully model the complete UV/O/NIR LC. We infer a total ^{56}Ni mass of $\sim 0.09 M_\odot$ and a total ejecta mass of 0.6 $M_\odot$. Ejecta velocities are $\leqslant 10^4$ km s^{-1}, in agreement with line velocities as measured from our spectral sequence.
4. SN 2022oqm is located in the spiral host galaxy NGC 5875 at an angular separation of 50$''$.6, corresponding to a projected physical distance of 13.1 kpc from the center of the galaxy and $\sim$2.4 half-light radii of the galaxy. We do not observe any obvious ongoing star formation at the location of the transient, with the nearest detected star-forming region $\approx$3 kpc away. Any progenitor system born in this star-forming region would require an average velocity $v = 147\frac{\text{km}}{\text{s}}\left[\frac{d}{3.0\ \text{kpc}}\right]\left[\frac{20\ \text{Myr}}{\tau}\right]$ over its entire lifetime τ.
5. While SN 2022oqm has similarities to SNe Ibc in terms of photometry (peak absolute magnitude) and spectroscopy (photospheric phase similarity to SNe Ic), the location of the SN in its host galaxy, inferred ejecta mass, and strong [Ca II] $\lambda\lambda$7291, 7324 feature are somewhat inconsistent with SNe Ibc. We find that, of the possible stripped-envelope SN populations, only Type Icn supernovae (SNe Icn) share some similarities with the observed properties of SN 2022oqm. SN 2019jc is the most similar SN Icn to SN 2022oqm, but significant differences persist between the two objects. Importantly, SN 2019jc is dominated by interactions between the SN ejecta and CSM throughout its evolution and much less ^{56}Ni than SN 2022oqm. As such, we suggest that if SN 2022oqm were an SESN, it may have resulted from a similar progenitor as SNe Icn, but with significantly less CSM and with a surprisingly large mass of ^{56}Ni produced.
6. We find that the detonation of an He layer on a white dwarf (WD) with mass $\gtrsim 0.6 M_\odot$ could also be consistent with the observed characteristics of SN 2022oqm. This WD progenitor of SN 2022oqm is surrounded by CSM that contains C and O, consistent with the disruption of a C/O WD binary companion progenitor. Ejecta mass and abundance constraints suggest that the WD could be an O/Ne WD or perhaps a massive C/O WD. Regardless, whether such massive WDs can have enough He to detonate in this method is not well constrained.

More detailed theoretical modeling of CaRT progenitors, focusing on massive hybrid WDs, could help further understand luminous CaRTs like SN 2022oqm. Alternatively, SN 2022oqm could present a link between SNe Ic and SNe Icn. Exploration of such a continuum, especially predictions on the correlations between CSM mass, SN ejecta mass and ^{56}Ni mass, could further explain the progenitor system of SN 2022oqm-like events. Such studies will also shed light on the full range of possible photometric and spectroscopic properties of CaRTs, allowing for much more comprehensive constraints on the space of possible CaRTs.

Acknowledgments

We thank Ido Irani and Avishay Gal-Yam for insightful feedback on modeling this object and interpreting the progenitor system. We thank Greg Zeimann for help with HET data reduction and Dan Weisz for Kast observations. S. K. Yadavalli and V. A. Villar acknowledge support by the NSF through grant AST-2108676. Much of the photometry and spectroscopy presented here were acquired as part of the ongoing Young Supernova Experiment (Jones et al. 2021; Aleo et al. 2023) The Young Supernova Experiment (YSE) and its research infrastructure is supported by the European Research Council under the European Union's Horizon 2020 research and innovation program (ERC grant Agreement 101002652, PI K. Mandel), the Heising-Simons Foundation (2018-0913, PI R. Foley; 2018-0911, PI R. Margutti), NASA (NNG17PX03C, PI R. Foley), NSF (AST-1720756, AST-1815935, PI R. Foley; AST-1909796, AST-1944985, PI R. Margutti), the David & Lucille Packard Foundation (PI R. Foley), VILLUM FONDEN (project 16599, PI J. Hjorth), and the Center for AstroPhysical Surveys (CAPS) at the National Center for Supercomputing Applications (NCSA) and the University of Illinois Urbana-Champaign. J.C.W. and J.V. acknowledge the support from the NSF grant AST-1813825. W.J.-G. is supported by the National Science Foundation Graduate Research Fellowship Program under grant No. DGE-1842165. W.J.-G. acknowledges support through NASA grants in support of Hubble Space Telescope program GO-16075 and 16500. C.D.K. is partly supported by a CIERA postdoctoral fellowship. D.A.C. acknowledges support from the National Science Foundation Graduate Research Fellowship under grant DGE1339067. C.R.A. was supported by a grant from VILLUM FONDEN (project No. 16599). D.F. is supported by a VILLUM FONDEN Young Investigator Grant (project No. 25501).

This project has been supported by the GINOP-2-3-2-15-2016-00033 project and the NKFIH/OTKA grants FK-134432 and K-142534 of the National Research, Development and

Innovation (NRDI) Office of Hungary, partly funded by the European Union. T.S. is supported by the János Bolyai Research Scholarship of the Hungarian Academy of Sciences, and by the New National Excellence Program (UNKP-22-5) of the Ministry for Culture and Innovation from the source of the NRDI Fund, Hungary. This project was supported by the KKP-137523 “SeismoLab” Élvonal grant of the Hungarian Research, Development and Innovation Office (NKFIH) and by the Lendület Program of the Hungarian Academy of Sciences under project No. LP2018-7.

This publication has made use of data collected at Lulin Observatory, partly supported by MoST grant 108-2112-M-008-001. We additionally acknowledge the use of public data from the Swift data archive. This work has made use of data from the Asteroid Terrestrial-impact Last Alert System (ATLAS) project. The Asteroid Terrestrial-impact Last Alert System (ATLAS) project is primarily funded to search for near-earth asteroids through NASA grants NN12AR55G, 80NSSC18K0284, and 80NSSC18K1575; byproducts of the NEO search include images and catalogs from the survey area. This work was partially funded by Kepler/K2 grant J1944/80NSSC19K0112 and HST GO-15889, and STFC grants ST/T000198/1 and ST/S006109/1. The ATLAS science products have been made possible through the contributions of the University of Hawaii Institute for Astronomy, the Queen’s University Belfast, the Space Telescope Science Institute, the South African Astronomical Observatory, and The Millennium Institute of Astrophysics (MAS), Chile. Y.Z. was partially supported by NASA TCAN and grant Nos. NNH17ZDA001N and TCAN-80NSSC18K1488. We acknowledge observations made with the Nordic Optical Telescope, owned in collaboration by the University of Turku and Aarhus University, and operated jointly by Aarhus University, the University of Turku, and the University of Oslo, representing Denmark, Finland, and Norway, the University of Iceland and Stockholm University at the Observatorio del Roque de los Muchachos, La Palma, Spain, of the Instituto de Astrofisica de Canarias. This work makes use of observations from the Las Cumbres Observatory global telescope network. The LCO group is supported by NSF grants AST-1911225 and AST0-1911151, and NASA Swift grant 80NSSC19K1639. This research has made use of the Spanish Virtual Observatory (https://svo.cab.inta-csic.es) project funded by MCIN/AEI/10.13039/501100011033/ through grant PID2020-112949GB-I00. The work of the Spanish Virtual Observatory’s Filter Profile Service has proven to be the backbone of using the proper filter bandpasses in proper photometric modeling. We cite them here (Rodrigo et al. 2012; Rodrigo & Solano 2020).

Facilities: PS1, Shane (Kast), Nickel, LCOGT, LO:1m, HET (LRS2), ARC (KOSMOS), ATLAS, Swift, KECK:II, PO:1.2m.

Software: `YSE-PZ` (Coulter et al. 2022, 2023), `MOSFiT` (Guillochon et al. 2018), `TARDIS` (Kerzendorf & Sim 2014), `extrabol` (Thornton & Villar 2022), `numpy` (Harris et al. 2020), `astropy`, (Astropy Collaboration et al. 2013, 2018, 2022), `matplotlib` (Hunter 2007), `scipy` (Virtanen et al. 2020).

Appendix A
All Known CaRTs

In Appendix A, we provide a list of all observed CaRTs at the time of publishing of this article in Table 5.

Table 5
Table of Every Known CaRT

Name	R.A.	Decl.	r-peak	Δm_7 (r)	Aliases	References
SN 2000ds	$09^{h}11^{m}36^{s}.24$	$+60^{\circ}01'42''.2$	⋯	⋯	⋯	Puckett & Dowdle (2000), Perets et al. (2010)
SN 2001co	$14^{h}19^{m}11^{s}.80$	$+24^{\circ}47'42''.9$	⋯	⋯	⋯	Aazami & Li (2001), Filippenko et al. (2003)
SN 2003H	$6^{h}16^{m}25^{s}.68$	$-21^{\circ}22'23''.8$	⋯	⋯	⋯	Hamuy (2003), Filippenko et al. (2003)
SN 2003dg	$11^{h}57^{m}31^{s}.97$	$-01^{\circ}15'13''.6$	⋯	⋯	⋯	Filippenko et al. (2003), Pugh & Li (2003)
SN2003dr	$14^{h}38^{m}11^{s}.13$	$46^{\circ}38'03''.4$	⋯	⋯	⋯	Filippenko et al. (2003), Puckett et al. (2003)
SN 2005cz	$12^{h}37^{m}27^{s}.85$	$74^{\circ}11'24''.5$	⋯	⋯	⋯	Dimai et al. (2005)
SN 2005E	$02^{h}39^{m}14^{s}.34$	$+01^{\circ}05'55''.0$	−15.53	0.55	⋯	Graham et al. (2005), Perets et al. (2010)
SN 2007ke	$02^{h}54^{m}23^{s}.90$	$+41^{\circ}24'16''.3$	−16.59	0.33	⋯	Chu et al. (2007), Perets et al. (2010) Kasliwal et al. (2012)
PTF09dav	$22^{h}46^{m}55^{s}.15$	$+21^{\circ}37'34''.1$	−16.22	0.49	⋯	Sullivan et al. (2011), Kasliwal et al. (2012)
SN 2010et	$17^{h}16^{m}54^{s}.27$	$+31^{\circ}33'51''.7$	−15.69	0.49	PTF10iuv	Kasliwal et al. (2012)
PTF10hcw	$08^{h}43^{m}36^{s}.22$	$+50^{\circ}12'38''.5$	⋯	⋯	⋯	Lunnan et al. (2017)
PTF11bij	$12^{h}58^{m}58^{s}.39$	$+37^{\circ}23'12''.0$	−15.68	0.45	⋯	Kasliwal et al. (2012)
PTF11kmb	$22^{h}22^{m}53^{s}.61$	$+36^{\circ}17'36''.5$	−15.57	0.28	⋯	Foley (2015), Lunnan et al. (2017)
SN 2012hn	$06^{h}42^{m}42^{s}.55$	$-27^{\circ}26'49''.8$	−15.55	0.14	⋯	Valenti et al. (2013)
PTF12bho	$13^{h}01^{m}16^{s}.65$	$+28^{\circ}01'18''.1$	−16.04	0.42	⋯	Lunnan et al. (2017)
iPTF15eqv	$10^{h}52^{m}11^{s}.40$	$+32^{\circ}57'01''$	⋯	⋯	⋯	Cao et al. (2015)
SN 2016hgs	$00^{h}50^{m}51^{s}.39$	$+27^{\circ}22'48''.0$	−15.45	0.42	iPTF16hgs	De et al. (2018a)
SN 2016hnk	$02^{h}13^{m}16^{s}.63$	$-07^{\circ}39'40''.80$	−17.05	0.32	ATLAS16dpc	Jacobson-Galán et al. (2020b)
SN 2018ckd	$14^{h}06^{m}11^{s}.95$	$-09^{\circ}20'39''.30$	−16.17	0.54	ZTF18aayhylv	De et al. (2020)
SN 2018gwo	$12^{h}08^{m}38^{s}.83$	$+68^{\circ}46'44''.40$	⋯	⋯	Gaia18dfp, PS19lf ZTF18acbwazl	De et al. (2020)
SN 2018gjx	$02^{h}16^{m}15^{s}.58$	$+28^{\circ}35'28''.64$	−17.51	0.68	ATLAS18vis, Gaia18csc kait-18ao, PS10do PSP18c, ZTF18abwkrbl	Das et al. (2022)
SN 2018jak	$09^{h}59^{m}18^{s}.20$	$+34^{\circ}53'43''.78$	−17.64	1.05	ATLAS18zqa, PS18clq ZTF18acqxyiq	Das et al. (2022)
SN 2018kjy	$06^{h}47^{m}17^{s}.96$	$+74^{\circ}14'05''.90$	−15.63	0.31	PS 18cfh, ZTF18acsodbf	De et al. (2020)
SN 2018lqo	$16^{h}28^{m}43^{s}.26$	$+41^{\circ}07'58''.70$	−16.21	0.41	ZTF18abmxelh	De et al. (2020)
SN 2018lqu	$15^{h}54^{m}11^{s}.48$	$+13^{\circ}30'50''.90$	⋯	⋯	ZTF18abttsrb	De et al. (2020)
SN 2019bkc	$10^{h}00^{m}22^{s}.54$	$-03^{\circ}01'12''.64$	−17.32	2.05	ATLAS19dqr	Tonry et al. (2019), Chen et al. (2020) Prentice et al. (2020), Zheng & Yu (2021)
SN 2019ehk	$12^{h}22^{m}56^{s}.15$	$+15^{\circ}49'34''.06$	−16.09	0.25	ATLAS19ibr, Gaia19bqn PS19ayq, ZTF19aatesgp	Jacobson-Galán et al. (2020a), De et al. (2021) Jacobson-Galán et al. (2021) Nakaoka et al. (2021), Das et al. (2022)
SN 2019hvg	$14^{h}06^{m}01^{s}.58$	$+12^{\circ}46'50''.38$	−16.7	0.23	ATLAS19bftc, ZTF19abacxod	Das et al. (2022)
SN 2019hty	$12^{h}55^{m}33^{s}.03$	$+32^{\circ}12'21''.70$	−16.38	0.33	ATLAS19nhp, PS 19bhn ZTF19aaznwze	De et al. (2020)
SN 2019ofm	$14^{h}50^{m}54^{s}.65$	$+27^{\circ}34'57''.60$	−17.03	0.34	ATLAS 19tjf, ZTF19abrdxbh	De et al. (2020)
SN 2019pof	$01^{h}12^{m}37^{s}.88$	$+33^{\circ}02'05''.75$	−15.94	0.53	ATLAS19uvh, PS19fbm ZTF19abxtcio	Das et al. (2022)
SN 2019pxu	$05^{h}10^{m}12^{s}.61$	$-00^{\circ}46'38''.60$	−16.56	0.30	ATLAS19uvg, PS19fwq ZTF19abwtqsk	De et al. (2020)
SN 2020sbw	$02^{h}46^{m}03^{s}.32$	$+03^{\circ}19'47''.67$	−17.1	0.31	ATLAS20yle, PS20hhn ZTF20abwzqzo	Das et al. (2022)
SN 2021M	$14^{h}14^{m}14^{s}.73$	$+35^{\circ}25'23''.14$	⋯	⋯	ATLAS21cum, ZTF21aaabwfu	Das et al. (2022)
SN 2021gno	$12^{h}12^{m}10^{s}.29$	$+13^{\circ}14'57''.04$	−15.44	0.83	ATLAS21iro, Gaia21cdw PS21cjz, ZTF21aaqhhfu	Jacobson-Galán et al. (2022), Ertini et al. (2023)
SN 2021inl	$13^{h}01^{m}33^{s}.24$	$+27^{\circ}49'55''.10$	−14.81	0.38	ATLAS21lqc, PS21dal ZTF21aasuego	Jacobson-Galán et al. (2022)
SN 2021pb	$09^{h}44^{m}46^{s}.80$	$+51^{\circ}41'14''.64$	−16.92	0.67	ZTF21aabxjqr	Das et al. (2022)
SN 2021sjt	$20^{h}37^{m}19^{s}.20$	$+66^{\circ}06'23''.13$	−15.00	0.44	ZTF21abjyiiw	Das et al. (2022)
SN 2022oqm	$15^{h}09^{m}12^{s}.09$	$+52^{\circ}32'05''.14$	−17.37	0.36	ZTF22aasxgjp	Irani et al. (2022), This Work

Notes. We present the R.A. and decl. in J2000 units, any known aliases, peak r-band absolute magnitude, ΔM_7 in r-band, and references for every CaRT. Objects with insufficient photometric coverage do not have r-band absolute magnitude and ΔM_7. We present references to detailed studies of objects, where available. Otherwise, we provide discovery and classification announcements of objects.

(This table is available in machine-readable form in the online article.)

Appendix B
Piro Model of Shock Cooling in `MOSFiT`

In addition to the power-law model of shock interaction presented in Section 5, we present a custom `MOSFiT` model of Shock Cooling-Double Radioactive decay, where we allow for diffusion of photons emitted by the shock interaction engine. Analogous to the presentation in Section 5.3, peak 1 would be modeled by the Piro model while peaks 2 and 3 are modeled with a ^{56}Ni radioactive decay model (Arnett 1982; Chatzopoulos et al. 2012). We find that allowing for photon diffusion results in poor agreement with peak 1, with reduced chi-squared of 29.1.

Appendix C
Photometric and Spectroscopic Observations

We present a fraction of the obtained photometry of SN 2022oqm in Table 6. All photometry presented here is in AB magnitudes and is not corrected for extinction or reddening. A portion of the data is shown here; full photometric dataset is provided via a machine-readable table. We also present a log of the spectroscopic observations in Table 7.

Table 6
Log of SN 2022oqm Spectra Presented in This Article

Time (MJD)	Phase (days)	Telescope	Instrument	Wavelength Range (Å)
59771.31	−12.86	Palomar 60 inch Telescope	SED Machine	3776–9223
59773.21	−10.96	Hobby Eberly Telescope	LRS2	3640–6950
59775.89	−8.28	Nordic Optical Telescope	ALFOSC	3800–8999
59776.31	−7.86	Hobby Eberly Telescope	LRS2	3640–9799
59777.20	−6.97	Hobby Eberly Telescope	LRS2	6450–10500
59779.26	−4.91	Keck II Telescope	NIRES	9538–24377
59779.27	−4.90	Shane 3 m Telescope	Kast	3303–10496
59780.27	−3.90	Shane 3 m Telescope	Kast	3508–10722
59784.19	0.02	Hobby Eberly Telescope	LRS2	3640–10500
59784.24	0.07	Shane 3 m Telescope	Kast	3503–10494
59788.25	4.08	Shane 3 m Telescope	Kast	3405–10495
59790.16	5.99	Hobby Eberly Telescope	LRS2	3640–10500
59793.16	8.99	Hobby Eberly Telescope	LRS2	3640–9700
59793.29	9.12	Shane 3 m Telescope	Kast	3253–10896
59798.28	14.11	Shane 3 m Telescope	Kast	3253–10894
59803.32	19.15	Faulkes Telescope North	FLOYDS	3459–9882
59809.23	25.06	Shane 3 m Telescope	Kast	3508–10730
59810.77	26.60	Faulkes Telescope North	FLOYDS	3459–9880
59814.22	30.05	Shane 3 m Telescope	Kast	3503–10893
59818.20	34.03	Shane 3 m Telescope	Kast	3253–10893
59824.20	40.03	Shane 3 m Telescope	Kast	3509–10703
59847.23	63.06	Keck I Telescope	LRIS	3120–10282

Notes. Phase is measured in days from time of *r*-band peak magnitude (MJD 59785). Note that the very first spectrum was presented on the Transient Name Server (Zimmerman et al. 2022) and we are presenting that spectrum as is.

(This table is available in machine-readable form in the online article.)

Table 7
Partial Log of SN 2022oqm Photometry Presented in This Article

Time (MJD)	Phase (days)	AB Magnitude	AB Magnitude Uncertainty	Telescope	Instrument	Band
59771.19	−13.81	17.323	0.038	P48	ZTF-Cam	*g*
59771.351	−13.649	17.499	0.048	Atlas	Atlas	*orange*
59771.54	−13.46	16.159	0.045	Swift	UVOT	*UVW1*
59771.54	−13.46	16.033	0.04	Swift	UVOT	*UVW2*
59771.54	−13.46	16.633	0.074	Swift	UVOT	*B*
59771.89	−13.11	17.28	0.1	Baja	Baja	*B*
59772.173	−12.827	17.033	0.052	Thacher	ACP	*g*
59772.205	−12.795	17.235	0.024	P48	ZTF-Cam	*r*
59772.241	−12.759	17.243	0.025	P48	ZTF-Cam	*r*
59772.259	−12.741	17.089	0.065	Nickel	Nickel	*B*
59772.27	−12.73	17.351	0.206	Swift	UVOT	*B*
59772.27	−12.73	16.95	0.076	Swift	UVOT	*U*

Notes. Phase is measured in days from time of *r*-band peak magnitude (MJD 59784.24). The complete photometry log is available as the data behind Figure 2.

ORCID iDs

S. Karthik Yadavalli https://orcid.org/0000-0002-0840-6940
V. Ashley Villar https://orcid.org/0000-0002-5814-4061
Luca Izzo https://orcid.org/0000-0001-9695-8472
Yossef Zenati https://orcid.org/0000-0002-0632-8897
Ryan J. Foley https://orcid.org/0000-0002-2445-5275
J. Craig Wheeler https://orcid.org/0000-0003-1349-6538
Charlotte R. Angus https://orcid.org/0000-0002-4269-7999
Katie Auchettl https://orcid.org/0000-0002-4449-9152
Attila Bódi https://orcid.org/0000-0002-8585-4544
Thomas de Boer https://orcid.org/0000-0001-5486-2747
Kenneth C. Chambers https://orcid.org/0000-0001-6965-7789
Ryan Chornock https://orcid.org/0000-0002-7706-5668
David A. Coulter https://orcid.org/0000-0003-4263-2228
Borbála Cseh https://orcid.org/0000-0002-6497-8863
Srujan Dandu https://orcid.org/0000-0003-4578-3216
Kyle W. Davis https://orcid.org/0000-0002-5680-4660
Connor Braden Dickinson https://orcid.org/0000-0001-9749-4200
Diego Farias https://orcid.org/0000-0001-7576-5428
Joseph Farah https://orcid.org/0000-0003-4914-5625
Christa Gall https://orcid.org/0000-0002-8526-3963
Hua Gao https://orcid.org/0000-0003-1015-5367
D. Andrew Howell https://orcid.org/0000-0003-4253-656X
Wynn V. Jacobson-Galan https://orcid.org/0000-0003-1103-3409
Nandita Khetan https://orcid.org/0000-0003-2720-8904
Charles D. Kilpatrick https://orcid.org/0000-0002-5740-7747
Réka Könyves-Tóth https://orcid.org/0000-0002-8770-6764
Levente Kriskovics https://orcid.org/0000-0002-1792-546X
Natalie LeBaron https://orcid.org/0000-0002-2249-0595
X. K. Le Saux https://orcid.org/0009-0004-3242-282X
Raffaella Margutti https://orcid.org/0000-0003-4768-7586
Eugene A. Magnier https://orcid.org/0000-0002-7965-2815
Curtis McCully https://orcid.org/0000-0001-5807-7893
Peter McGill https://orcid.org/0000-0002-1052-6749
Hao-Yu Miao https://orcid.org/0000-0003-2736-5977
Megan Newsome https://orcid.org/0000-0001-9570-0584
Estefania Padilla Gonzalez https://orcid.org/0000-0003-0209-9246
András Pál https://orcid.org/0000-0001-5449-2467
Yen-Chen Pan https://orcid.org/0000-0001-8415-6720
Collin A. Politsch https://orcid.org/0000-0003-3727-9167
Conor L. Ransome https://orcid.org/0000-0003-4175-4960
Enrico Ramirez-Ruiz https://orcid.org/0000-0003-2558-3102
Armin Rest https://orcid.org/0000-0002-4410-5387
Sofia Rest https://orcid.org/0000-0002-3825-0553
Huei Sears https://orcid.org/0000-0001-8023-4912
Jackson Scheer https://orcid.org/0000-0002-3522-6312
Ádám Sódor https://orcid.org/0000-0001-7806-2883
Jonathan Swift https://orcid.org/0000-0002-9486-818X
Róbert Szakáts https://orcid.org/0000-0002-1698-605X
Tamás Szalai https://orcid.org/0000-0003-4610-1117
Kirsty Taggart https://orcid.org/0000-0002-5748-4558
Giacomo Terreran https://orcid.org/0000-0003-0794-5982
Padma Venkatraman https://orcid.org/0000-0001-8638-2780
József Vinkó https://orcid.org/0000-0001-8764-7832
Grace Yang https://orcid.org/0000-0001-7823-2627
Henry Zhou https://orcid.org/0000-0002-2093-6960

References

Aazami, A., & Li, W. 2001, IAUC, 7643, 2
Abazajian, K., Adelman-McCarthy, J. K., Agüeros, M. A., et al. 2005, AJ, 129, 1755
Aleo, P. D., Malanchev, K., Sharief, S., et al. 2023, ApJS, 266, 9
Arnett, W. D. 1982, ApJ, 253, 785
Astropy Collaboration, Price-Whelan, A. M., Lim, P. L., et al. 2022, ApJ, 935, 167
Astropy Collaboration, Price-Whelan, A. M., Sipőcz, B. M., et al. 2018, AJ, 156, 123
Astropy Collaboration, Robitaille, T. P., Tollerud, E. J., et al. 2013, A&A, 558, A33
Becker, A., 2015 HOTPANTS: High Order Transform of PSF ANd Template Subtraction, Astrophysics Source Code Library, ascl:1504.004
Bellm, E. C., Kulkarni, S. R., Graham, M. J., et al. 2019, PASP, 131, 018002
Bersten, M. C., Benvenuto, O. G., Folatelli, G., et al. 2014, AJ, 148, 68
Bertin, E., 2010 SWarp: Resampling and Co-adding FITS Images Together, Astrophysics Source Code Library, ascl:1010.068
Betoule, M., Kessler, R., Guy, J., et al. 2014, A&A, 568, A22
Blanchard, P. K., Berger, E., & Fong, W.-f. 2016, ApJ, 817, 144
Bobrick, A., Zenati, Y., Perets, H. B., Davies, M. B., & Church, R. 2022, MNRAS, 510, 3758
Boyle, A., Sim, S. A., Hachinger, S., & Kerzendorf, W. 2017, A&A, 599, A46
Branch, D., Doggett, J. B., Nomoto, K., & Thielemann, F. K. 1985, ApJ, 294, 619
Brown, P. J., Breeveld, A. A., Holland, S., Kuin, P., & Pritchard, T. 2014, Ap&SS, 354, 89
Burmester, U. P., Ferrario, L., Pakmor, R., et al. 2023, MNRAS, 523, 527
Burrows, D. N., Hill, J. E., Nousek, J. A., et al. 2005, SSRv, 120, 165
Cao, Y., Kasliwal, M. M., Arcavi, I., et al. 2013, ApJL, 775, L7
Cao, Y., Kulkarni, S. R., Cook, D., & Vreeswijk, P. 2015, ATel, 8428, 1
Chambers, K. C., Huber, M. E., Flewelling, H., et al. 2017, TNSTR 2017-324
Chatzopoulos, E., Wheeler, J. C., & Vinko, J. 2012, ApJ, 746, 121
Chen, P., Dong, S., Stritzinger, M. D., et al. 2020, ApJL, 889, L6
Chu, J., Li, W., Kloehr, W., Mikuz, H., & Yuan, F. 2007, IAUC, 8875, 2
Coulter, D. A., Jones, D. O., McGill, P., et al. 2022, YSE-PZ: An Open-source Target and Observation Management System v0.3.0, Zenodo, doi:10.5281/zenodo.7278430
Coulter, D. A., Jones, D. O., McGill, P., et al. 2023, PASP, 135, 064501
Cushing, M. C., Vacca, W. D., & Rayner, J. T. 2004, PASP, 116, 362
Dan, M., Rosswog, S., Guillochon, J., & Ramirez-Ruiz, E. 2011, ApJ, 737, 89
Dan, M., Rosswog, S., Guillochon, J., & Ramirez-Ruiz, E. 2012, MNRAS, 422, 2417
Das, K. K., Kasliwal, M. M., Fremling, C., et al. 2023, ApJ, 959, 12
Davis, K. W., Taggart, K., Tinyanont, S., et al. 2023, MNRAS, 523, 2530
De, K., Fremling, U. C., Gal-Yam, A., et al. 2021, ApJL, 907, L18
De, K., Kasliwal, M. M., Cantwell, T., et al. 2018a, ApJ, 866, 72
De, K., Kasliwal, M. M., Ofek, E. O., et al. 2018b, Sci, 362, 201
De, K., Kasliwal, M. M., Tzanidakis, A., et al. 2020, ApJ, 905, 58
Dessart, L., Burrows, A., Livne, E., & Ott, C. D. 2007, ApJ, 669, 585
Dessart, L., & Hillier, D. J. 2015, MNRAS, 447, 1370
Dimai, A., Sehgal, A., Newton, J., et al. 2005, IAUC, 8569, 1
Drout, M. R., Soderberg, A. M., Gal-Yam, A., et al. 2011, ApJ, 741, 97
Ertini, K., Folatelli, G., Martinez, L., et al. 2023, MNRAS, 526, 279
Fernández, R., Margalit, B., & Metzger, B. D. 2019, MNRAS, 488, 259
Fernández, R., & Metzger, B. D. 2013, ApJ, 763, 108
Filippenko, A. V., Barth, A. J., Matheson, T., et al. 1995, ApJL, 450, L11
Filippenko, A. V., Chornock, R., Swift, B., et al. 2003, IAUC, 8159, 2
Fink, M., Hillebrandt, W., & Röpke, F. K. 2007, A&A, 476, 1133
Fink, M., Röpke, F. K., Hillebrandt, W., et al. 2010, A&A, 514, A53
Flewelling, H. A., Magnier, E. A., Chambers, K. C., et al. 2020, ApJS, 251, 7
Foley, R. J. 2015, MNRAS, 452, 2463
Foley, R. J., Challis, P. J., Chornock, R., et al. 2013, ApJ, 767, 57
Foley, R. J., Papenkova, M. S., Swift, B. J., et al. 2003, PASP, 115, 1220
Fruchter, A. S., Levan, A. J., Strolger, L., et al. 2006, Natur, 441, 463
Fulton, M., Huber, M. E., Tucker, M. A., et al. 2022, TNSCR, 2022-2169
Galbany, L., Ashall, C., Höflich, P., et al. 2019, A&A, 630, A76
Gal-Yam, A., Bruch, R., Schulze, S., et al. 2022, Natur, 601, 201
Gal-Yam, A., Yaron, O., Pastorello, A., et al. 2021, TNSAN, 76, 1
Gaskell, C. M., Cappellaro, E., Dinerstein, H. L., et al. 1986, ApJL, 306, L77
Gehrels, N., Chincarini, G., Giommi, P., et al. 2004, ApJ, 611, 1005
Gelman, A., Hwang, J., & Vehtari, A. 2014, Statistics and Computing, 24, 997
Graham, J., Li, W., Schwartz, M., & Trondal, O. 2005, IAUC, 8465, 1
Guillochon, J., Dan, M., Ramirez-Ruiz, E., & Rosswog, S. 2010, ApJL, 709, L64

Guillochon, J., Nicholl, M., Villar, V. A., et al. 2018, ApJS, 236, 6

Habergham, S. M., Anderson, J. P., James, P. A., & Lyman, J. D. 2014, MNRAS, 441, 2230

Hamuy, M. 2003, IAUC, 8045, 3

Harris, C. R., Millman, K. J., van der Walt, S. J., et al. 2020, Natur, 585, 357

HI4PI Collaboration, Ben Bekhti, N., Flöer, L., et al. 2016, A&A, 594, A116

Holcomb, C., Guillochon, J., De Colle, F., & Ramirez-Ruiz, E. 2013, ApJ, 771, 14

Horne, K. 1986, PASP, 98, 609

Hunter, D. J., Valenti, S., Kotak, R., et al. 2009, A&A, 508, 371

Hunter, J. D. 2007, CSE, 9, 90

Irani, I., Chen, P., Morag, J., et al. 2024, ApJ, 963, 109

Iwamoto, K., Nomoto, K., Höflich, P., et al. 1994, ApJL, 437, L115

Jacobson-Galán, W. V., Margutti, R., Kilpatrick, C. D., et al. 2020a, ApJ, 898, 166

Jacobson-Galán, W. V., Margutti, R., Kilpatrick, C. D., et al. 2021, ApJL, 908, L32

Jacobson-Galán, W. V., Polin, A., Foley, R. J., et al. 2020b, ApJ, 896, 165

Jacobson-Galán, W. V., Venkatraman, P., Margutti, R., et al. 2022, ApJ, 932, 58

Jones, D. O., Foley, R. J., Narayan, G., et al. 2021, ApJ, 908, 143

Kaiser, N., Aussel, H., Burke, B. E., et al. 2002, Proc. SPIE, 4836, 154

Kaltenborn, M. A., Fryer, C. L., Wollaeger, R. T., et al. 2023, ApJ, 956, 71

Kasen, D., & Bildsten, L. 2010, ApJ, 717, 245

Kasliwal, M. M., Kulkarni, S. R., Gal-Yam, A., et al. 2012, ApJ, 755, 161

Kawabata, M., Maeda, K., Yamanaka, M., et al. 2021, PASJ, 73, 1295

Kelly, P. L., & Kirshner, R. P. 2012, ApJ, 759, 107

Kerzendorf, W. E., & Sim, S. A. 2014, MNRAS, 440, 387

Landolt, A. U. 1992, AJ, 104, 372

Leadbeater, R. 2022, TNSCR, 2022-2126

Leloudas, G., Dai, L., Arcavi, I., et al. 2019, ApJ, 887, 218

Lucy, L. 2002, A&A, 384, 725

Lunnan, R., Kasliwal, M. M., Cao, Y., et al. 2017, ApJ, 836, 60

Maeda, K., Mazzali, P. A., Deng, J., et al. 2003, ApJ, 593, 931

Magnier, E. A., Schlafly, E. F., Finkbeiner, D. P., et al. 2020, ApJS, 251, 6

McCully, C., Jha, S. W., Scalzo, R. A., et al. 2022, ApJ, 925, 138

Meng, X., & Han, Z. 2015, A&A, 573, A57

Metzger, B. D., Piro, A. L., & Quataert, E. 2008, MNRAS, 390, 781

Metzger, B. D., Piro, A. L., & Quataert, E. 2009, MNRAS, 396, 1659

Milisavljevic, D., Patnaude, D. J., Raymond, J. C., et al. 2017, ApJ, 846, 50

Miller, J. S., & Stone, R. P. S. 1993, The Kast Double Spectrograph No. 66, University of California, https://mthamilton.ucolick.org/techdocs/instruments/kast/Tech%20Report%2066%20KAST%20Miller%20Stone.pdf

Miyaji, S., Nomoto, K., Yokoi, K., & Sugimoto, D. 1980, PASJ, 32, 303

Modjaz, M., Li, W., Butler, N., et al. 2009, ApJ, 702, 226

Modjaz, M., Liu, Y. Q., Bianco, F. B., & Graur, O. 2016, ApJ, 832, 108

Moffat, A. F. J. 1969, A&A, 3, 455

Möller, A., Peloton, J., Ishida, E. E. O., et al. 2021, MNRAS, 501, 3272

Morag, J., Sapir, N., & Waxman, E. 2023, MNRAS, 522, 2764

Nakaoka, T., Maeda, K., Yamanaka, M., et al. 2021, ApJ, 912, 30

Nakar, E., & Sari, R. 2010, ApJ, 725, 904

Nicholl, M., Guillochon, J., & Berger, E. 2017, ApJ, 850, 55

Nomoto, K. 1982, ApJ, 257, 780

Nomoto, K., Thielemann, F. K., & Yokoi, K. 1984, ApJ, 286, 644

Nugent, P., Kim, A., & Perlmutter, S. 2002, PASP, 114, 803

Oke, J. B., Cohen, J. G., Carr, M., et al. 1995, PASP, 107, 375

Ostriker, J. P., & Gunn, J. E. 1971, ApJL, 164, L95

Pakmor, R., Zenati, Y., Perets, H. B., & Toonen, S. 2021, MNRAS, 503, 4734

Pastorello, A., Vogl, C., Taubenberger, S., et al. 2021, TNSAN, 71, 1

Pellegrino, C., Howell, D. A., Terreran, G., et al. 2022, ApJ, 938, 73

Perets, H. B., & Beniamini, P. 2021, MNRAS, 503, 5997

Perets, H. B., Gal-Yam, A., Mazzali, P. A., et al. 2010, Natur, 465, 322

Perets, H. B., Zenati, Y., Toonen, S., & Bobrick, A. 2019, arXiv:1910.07532

Perley, D., Chu, M., Dahiwale, A., & Fremling, C. 2022, TNSCR 2022-2131, 1

Perley, D. A., Fremling, C., Sollerman, J., et al. 2020, ApJ, 904, 35

Perley, D. A., Sollerman, J., Schulze, S., et al. 2022, ApJ, 927, 180

Phillips, M. M. 1993, ApJL, 413, L105

Piro, A. L., Haynie, A., & Yao, Y. 2021, ApJ, 909, 209

Piro, A. L., & Kulkarni, S. R. 2013, ApJL, 762, L17

Planck Collaboration, Ade, P. A. R., Aghanim, N., et al. 2016, A&A, 594, A13

Prentice, S. J., Maguire, K., Flörs, A., et al. 2020, A&A, 635, A186

Puckett, T., & Dowdle, G. 2000, IAUC, 7507, 2

Puckett, T., Toth, D., Schwartz, M., et al. 2003, IAUC, 8117, 1

Pugh, H., & Li, W. 2003, IAUC, 8113, 2

Quimby, R. M., Wheeler, J. C., Höflich, P., et al. 2007, ApJ, 666, 1093

Ransome, C. L., Habergham-Mawson, S. M., Darnley, M. J., James, P. A., & Percival, S. M. 2022, MNRAS, 513, 3564

Rest, A., Stubbs, C., Becker, A. C., et al. 2005, ApJ, 634, 1103

Rest, S., Rest, A., Wang, Q., et al. 2023, ATClean: High-Fidelity, Statistically Clean ATLAS Light Curves and Feature Detection v2, Zenodo, doi:10.5281/zenodo.7897345

Rodrigo, C., & Solano, E. 2020, in Scientific Meeting of the Spanish Astronomical Society 14, 182

Rodrigo, C., Solano, E., & Bayo, A. 2012 Oct, IVOA Working Draft 15 October 2012, 1015

Roming, P. W. A., Kennedy, T. E., Mason, K. O., et al. 2005, SSRv, 120, 95

Sawada, R., Kashiyama, K., & Suwa, Y. 2022, ApJ, 927, 223

Schechter, P. L., Mateo, M., & Saha, A. 1993, PASP, 105, 1342

Schlafly, E. F., & Finkbeiner, D. P. 2011, ApJ, 737, 103

Schulze, S., Yaron, O., Sollerman, J., et al. 2021, ApJS, 255, 29

Schwab, J. 2021, ApJ, 906, 53

Shen, K. J., Kasen, D., Weinberg, N. N., Bildsten, L., & Scannapieco, E. 2010, ApJ, 715, 767

Shen, K. J., Quataert, E., & Pakmor, R. 2019, ApJ, 887, 180

Shingles, L., Smith, K. W., Young, D. R., et al. 2021, TNSAN, 7, 1

Shivvers, I., Filippenko, A. V., Silverman, J. M., et al. 2019, MNRAS, 482, 1545

Siebert, M. R., Dimitriadis, G., Polin, A., & Foley, R. J. 2020, ApJL, 900, L27

Siebert, M. R., Foley, R. J., Jones, D. O., et al. 2019, MNRAS, 486, 5785

Silverman, J. M., Foley, R. J., Filippenko, A. V., et al. 2012b, MNRAS, 425, 1789

Silverman, J. M., Ganeshalingam, M., Li, W., & Filippenko, A. V. 2012a, MNRAS, 425, 1889

Smith, J. A., Tucker, D. L., Kent, S., et al. 2002, AJ, 123, 2121

Smith, K. W., Smartt, S. J., Young, D. R., et al. 2020, PASP, 132, 085002

Smith, N. 2017, in Handbook of Supernovae, ed. A. W. Alsabti & P. Murdin (Berlin: Springer), 403

Sollerman, J., Zimmerman, E., Irani, I., et al. 2022, TNSTR, 2022-1948

Stritzinger, M. D., Valenti, S., Hoeflich, P., et al. 2015, A&A, 573, A2

Sullivan, M., Kasliwal, M., Nugent, P., et al. 2011, ApJ, 732, 118

Swift, J. J., Andersen, K., Arculli, T., et al. 2022, PASP, 134, 035005

Taubenberger, S., Pastorello, A., Mazzali, P. A., et al. 2006, MNRAS, 371, 1459

Tauris, T. M., Langer, N., & Podsiadlowski, P. 2015, MNRAS, 451, 2123

Thornton, I., & Villar, A. 2022, villrv/extrabol: Zenodo Release v1.0.0, Zenodo, doi:10.5281/zenodo.7261669

Tinyanont, S., Ridden-Harper, R., Foley, R. J., et al. 2021, MNRAS, 512, 2777

Tonry, J., Denneau, L., Heinze, A., et al. 2019, TNSTR, 2019-310

Tonry, J. L., Denneau, L., Heinze, A. N., et al. 2018, PASP, 130, 064505

Tripp, R., & Branch, D. 1999, ApJ, 525, 209

Tully, R. B., Courtois, H. M., Dolphin, A. E., et al. 2013, AJ, 146, 86

Vacca, W. D., Cushing, M. C., & Rayner, J. T. 2003, PASP, 115, 389

Valenti, S., Elias-Rosa, N., Taubenberger, S., et al. 2008, ApJL, 673, L155

Valenti, S., Howell, D., Stritzinger, M., et al. 2016, MNRAS, 459, 3939

Valenti, S., Yuan, F., Taubenberger, S., et al. 2013, MNRAS, 437, 1519

van Driel, W., Butcher, Z., Schneider, S., et al. 2016, A&A, 595, A118

Villar, V. A., Berger, E., Metzger, B. D., & Guillochon, J. 2017, ApJ, 849 70

Virtanen, P., Gommers, R., Oliphant, T. E., et al. 2020, NatMe, 17, 261

Waldman, R., Sauer, D., Livne, E., et al. 2011, ApJ, 738, 21

Watanabe, S. 2013, The Journal of Machine Learning Research, 14, 867

Waters, C. Z., Magnier, E. A., Price, P. A., et al. 2020, ApJS, 251, 4

Williamson, M., Kerzendorf, W., & Modjaz, M. 2021, ApJ, 908, 150

Wilson, J. C., Henderson, C. P., Herter, T. L., et al. 2004, Proc. SPIE, 5492, 1295

Woosley, S., & Kasen, D. 2011, ApJ, 734, 38

Woosley, S. E. 2010, ApJL, 719, L204

Wu, C., Xiong, H., & Wang, X. 2022, MNRAS, 512, 2972

Yao, Y., De, K., Kasliwal, M. M., et al. 2020, ApJ, 900, 46

Zenati, Y., Bobrick, A., & Perets, H. B. 2020, MNRAS, 493, 3956

Zenati, Y., Perets, H. B., Dessart, L., et al. 2023, ApJ, 944, 22

Zenati, Y., Perets, H. B., & Toonen, S. 2019a, MNRAS, 486, 1805

Zenati, Y., Toonen, S., & Perets, H. B. 2019b, MNRAS, 482, 1135

Zheng, J.-H., & Yu, Y.-W. 2021, RAA, 21, 200

Zimmerman, E., Irani, I., Chen, P., et al. 2022, TNSCR, 2022-1951